Journal of
Materials Chemistry A

PAPER

View Article Online
View Journal

Cite this: DOI: 10.1039/d5ta09345g

Vapor-phase pillarization of MXenes for engineering hierarchical interlayer porosity

Song Luo,†[a] Ali Kamali,†[a] Joshua M. Little,[b] Akash Warty,[a] Jong K. Keum,[c] Po-Yen Chen,[b] Yeonsu Kwak,[a] Hyunjik K. Kim,[a] Dionisios G. Vlachos,[a] Ke Zhang,[d] John Yang[d] and Dongxia Liu*[a]

Received 18th November 2025
Accepted 9th April 2026

DOI: 10.1039/d5ta09345g

rsc.li/materials-a

MXenes, a family of two-dimensional (2D) multilamellar materials, possess excellent thermal and electronic properties for a range of applications. Their use in heterogeneous catalysis, however, is limited by the low surface area resulting from stacked layers. Pillarization with inorganic oxides can create more open, mesoporous MXene structures, improving accessibility for guest species to diffuse, reside or react in the space between 2D layers. A previous liquid-phase pillarization method, however, involves excessive use of solvent-based precursors and multiple processing steps. Here, we report a vapor-phase pillarization (VPP) strategy to introduce pillars, exemplified by silica pillars, with high pillar precursor usage efficiency and a simplified processing workflow. The resulting silica-pillared mesoporous MXene exhibits significantly increased surface area and porosity. These textural properties can be easily tuned by the VPP synthesis conditions. When applied as a ruthenium (Ru) catalyst support for the hydrogenolysis of low-density polyethylene (LDPE), the silica-pillared MXene enabled high Ru dispersion and catalytic activity. This study highlights the potential of the VPP method for engineering mesoporous, 2D MXene materials and demonstrates the effectiveness of mesoporous MXene as a catalyst support in overcoming mass transport and active-site accessibility challenges in heterogeneous catalysis involving bulky substances, such as plastics upcycling.

1. Introduction

MXenes are a family of two-dimensional (2D), multilamellar materials first reported in 2011.[1] With the general formula $M_{n+1}X_nT_x$, MXenes consist of alternating layers: an M layer composed of early transition metals (*e.g.*, Ti, V, or Cr) and an X layer made of carbon (C) and/or nitrogen (N). The T_x term represents surface functional groups (typically O, OH, F, or Cl (ref. 2–7)) that result from the synthesis processes. Due to their excellent thermal and electronic properties, MXenes have been explored for diverse applications, including batteries,[8,9] supercapacitors,[10] fuel cells,[11,12] energy storage,[13–18] and catalysis.[19–21] However, their use as catalyst supports in heterogeneous catalysis remains limited by structural challenges. In particular, the stacked architecture of MXene sheets results in low surface areas (typically 4–20 $m^2\ g^{-1}$).[22,23] The densely packed 2D layers hinder the dispersion and accessibility of guest metal particles between sheets. This also impedes reactant access to the interlayer space and limits mass transport. These challenges are especially pronounced in reactions involving bulky molecules, such as those encountered in plastics upcycling.

Delamination and pillarization strategies have been employed to increase interlayer spacing in MXenes and address the aforementioned structural limitations. In delamination, cations (*e.g.*, tetramethylammonium ions, Li^+) or organic molecules (*e.g.*, urea and isopropylamine) are intercalated between MXene layers, followed by agitation or sonication to exfoliate the sheets into isolated nanosheets.[24–27] However, these delaminated layers often tend to re-stack, resulting in surface areas comparable to those of pristine MXene.[24] In contrast, pillarization introduces foreign species such as inorganic oxides or metal species between MXene layers to prevent re-stacking and enhance both interlayer spacing and surface area. This is typically achieved either after intercalation or *via* vacuum-assisted self-assembly of delaminated nanosheets. For example, Bimbo *et al.*[8,9] intercalated dodecylamine (DDA) and tetraethyl orthosilicate (TEOS) into MXene multilayers, followed by TEOS hydrolysis to form silica (SiO_2) pillars. Chen *et al.*[28] mixed $Ti_3C_2T_x$ nanosheets with pre-synthesized SiO_2 nanoparticles and assembled them to form SiO_2-pillared MXene *via* a vacuum-assisted process. Similarly, Tao *et al.*[29] used cetyltrimethylammonium bromide (CTAB) and $SnCl_4$ to produce Sn^{4+}-

---

[a] *Department of Chemical and Biomolecular Engineering, University of Delaware, Delaware, DE 19716, USA. E-mail: liud@udel.edu; Tel: (+1) 301-405-3522*

[b] *Department of Chemical and Biomolecular Engineering, University of Maryland, College Park, MD 20742, USA*

[c] *Center for Nanophase Materials Sciences and Neutron Scattering Division, Oak Ridge National Laboratory, Oak Ridge, TN 37830, USA*

[d] *Aramco Research Center – Houston, Saudi Aramco, Houston, TX 77077, USA*

† These authors contributed equally.

pillared MXene, while Zhang *et al.*[30] employed $SbCl_3$ to synthesize Sb-pillared MXene. It should be noted that all of these methods rely on liquid-phase processing, which involves excessive solvent use, generates significant liquid waste, and requires separation steps to recover solid products. Moreover, the resulting pillared MXenes have primarily been explored for electrochemical applications, such as batteries and capacitors.

Here, we report a vapor-phase pillarization (VPP) strategy to engineer hierarchical porosity in MXenes through the formation of silica-pillared MXene structures. VPP of 2D materials was first introduced by our group for pillaring 2D zeolites.[31] Unlike traditional liquid-phase pillarization (LPP), the VPP method requires ∼10 times less silica precursor (*e.g.*, TEOS) and enables ∼100% utilization of the alkoxide.[32–36] Since no liquid phase is involved, separation and recovery steps are eliminated, simplifying the process and improving efficiency. In this study, we extend the VPP approach to MXenes, which are compositionally different from silica-based zeolites. We investigated the effects of various pillarization parameters, including TEOS loading, the amount of swelling agent, the water content for TEOS hydrolysis, and the pillarization temperature. The resulting SiO_2-pillared MXene exhibits hierarchical porosity arising from controlled interlayer engineering. To demonstrate the functional implications of the engineered porosity, the SiO_2-pillared MXene was evaluated as a mesoporous support for ruthenium (Ru) in a representative catalytic reaction involving bulky molecules. Specifically, in the hydrogenolysis of low-density polyethylene (LDPE), the SiO_2-pillared MXene-supported Ru catalyst showed significantly enhanced activity compared to Ru supported on unpillared MXene with equivalent metal loading. This improvement is attributed to the hierarchical pore architecture, which better accommodates large polymer chains and facilitates molecular transport within the catalytic matrix. The present work demonstrates VPP as an effective structural engineering strategy for increasing hierarchical porosity in MXene materials, thereby expanding their potential utility in applications where mass-transport limitations are critical.

2. Experimental

2.1 Materials

Hydrochloric acid (HCl, 37%), lithium fluoride (LiF, ≥99.9%), dodecylamine (DDA, 98%), octadecylamine (ODA, 98%), hexylamine (HA, 99%), hexaammineruthenium(II) chloride ($[Ru(NH_3)_6]Cl_2$), and low-density polyethylene (LDPE, Mw ∼4 kDa) were purchased from Sigma-Aldrich. Ti_3AlC_2 MAX powder was obtained from Tongrun Info Technology Co. Ltd, China. Tetraethyl orthosilicate (TEOS, 98%) was purchased from Alfa Aesar. Deionized (DI) water was used in the experiment.

2.2 Material synthesis

2.2.1 Synthesis of the 2D MXene material. $Ti_3C_2T_x$ MXene nanosheets were synthesized by selectively etching the Al layer from the Ti_3AlC_2 MAX phase, following a reported procedure.[37,38] Specifically, 1.0 g of Ti_3AlC_2 MAX powder was added to a mixture of 40 mL of 9.0 M HCl solution and 3.0 g of LiF (*Caution! HF might be generated in this step, which is extremely hazardous and toxic. Hence, this step should ALWAYS be performed in a hood with special gloves and a lab coat designed exclusively for handling HF*). The mixture was stirred magnetically at 35 °C for 24 h at 400 rpm. After etching, the resulting suspension was centrifuged at 8000 rpm for 5 min. Following decantation of the supernatant, cold 2.0 M HCl was added to the precipitate and mixed to form a suspension. This centrifugation-decantation-redispersion process in cold HCl was repeated three times to remove residual ions and byproducts. The HCl solution was then replaced with DI water, and the washing process was repeated until the suspension reached a pH of ∼6.0. Subsequently, the mixture was sonicated for 60 min to produce delamination, followed by centrifugation at 3000 rpm for 30 min. The delaminated $Ti_3C_2T_x$ nanosheets (MXene) in the supernatant were collected by lyophilization using a freeze dryer (Labconco FreeZone) at −85 °C and 101 Pa pressure for further synthesis and characterization.

2.2.2 Synthesis of the 2D P-MXene material. The experimental setup for the pillarization of MXene using the VPP method follows our previously reported procedure for VPP of 2D zeolites.[39] In a typical process, proper amounts of MXene and an amine swelling agent were added to a glass vial. After mixing the two materials, the vial was transferred into a 50 mL Teflon liner, which was then placed within a stainless-steel autoclave. Subsequently, TEOS was added to the Teflon liner, outside the glass vial. The autoclave was sealed and placed in a preheated oven at the target temperature for 24 h. The autoclave was then removed from the oven and allowed to cool in a fume hood. A proper amount of water was added to the space between the outer wall of the glass vial and the inner wall of the Teflon liner. The autoclave was sealed again and heated in an oven preheated to 80 °C for another 24 h. After cooling, the material in the glass vial was transferred into a furnace (Lindberg/Blue M™, TF55030 A-1) for calcination. The calcination process involved ramping from ambient temperature to 400 °C at a rate of 0.8 °C min^{-1}, followed by holding at the final temperature for 12 h under a N_2 gas (Purity: 99.999%; Airgas) flow of 100 mL min^{-1}. This synthesized pillared MXene material is named "P-MXene".

2.2.3 Synthesis of MXene or P-MXene supported Ru catalysts. The MXene-supported Ru catalyst (*i.e.*, Ru@MXene) was synthesized by adding 5.2 g of a 0.1 M hexaammineruthenium(II) chloride solution to 1 g MXene, followed by mixing at 500 rpm for 60 min. The resulting mixture was then lyophilized using a freeze dryer (Labconco FreeZone) at −85 °C and 101 Pa pressure. After freeze drying, the sample was reduced in a tubular furnace at 300 °C for 2 h at a ramp rate 5 °C min^{-1} under a 5% H_2/N_2 gas mixture flowing at 100 mL min^{-1}. The P-MXene-supported Ru (*i.e.*, Ru@P-MXene) catalyst was prepared using an incipient wetness impregnation approach. First, a $[Ru(NH_3)_6]Cl_2$ stock solution (0.1 mol L^{-1}) was added in a dropwise fashion to the prepared P-MXene, and then it was dried at 60 °C in a vacuum oven for 2 h. Finally, the prepared Ru@P-MXene sample was also reduced according to the same method as Ru@P-MXene. The Ru loading in Ru@MXene or Ru@P-MXene was 5 wt%, and both catalysts were ready for catalytic testing.

2.3 Materials characterization

X-ray diffraction (XRD) measurements were conducted on a Bruker D8 diffractometer with Cu Kα radiation ($\lambda = 1.54$ Å) over a 2θ range of 15–40°. For diffraction angles below 15°, small-angle X-ray scattering (SAXS) was performed using a Xenocs Xeuss 3.0 instrument equipped with a D2 + MetalJet X-ray source (Ga Kα, 9.2 keV, $\lambda = 1.34$ Å). N_2 adsorption–desorption isotherms were collected at −196.15 °C using a Micromeritics 3Flex surface characterization analyzer. Prior to measurements, the samples were degassed at 130 °C under vacuum for 16 h. The pore size distribution and cumulative pore volume were determined by density functional theory (DFT) based on the adsorption branch of the isotherms. The total and micropore surface areas were calculated by the Brunauer–Emmett–Teller (BET; using the adsorption branch of the N_2 isotherm data, $P/P_0 = 0.05–0.35$) and t-plot methods ($P/P_0 < 0.1$), respectively. The mesopore surface area was obtained by subtracting the micropore surface area from the BET surface area. The micropore volume was taken from the cumulative pore volume at pore sizes <2 nm, the mesopore volume from the cumulative pore volume between 2–50 nm, and the macropore volume from pore sizes >50 nm, based on the cumulative pore volume distribution. Morphological features of the samples were characterized by scanning electron microscopy (SEM, Zeiss Merlin) and transmission electron microscopy (TEM, JEOL JEM-2010F). Raman spectra were acquired using a Raman spectrometer (LabRAM HR Evolution, Horiba Scientific, Japan), and the measuring conditions include an acquisition time of 10 s, three accumulations, RTD time of 1 s, excitation at 532 nm, neutral density filter set to 3.2%, confocal hole size of 200, and a 600 lines per mm grating (500 nm) in the visible range. The instrument was calibrated using the Si Raman peak at 520.8 cm^{-1}. For the sample preparation, the dried powder was sandwiched between two glass microscope slides and pressed to obtain flat MAX or MXene particles. X-ray photoelectron spectroscopy (XPS) was performed using a Kratos Axis Supra + spectrometer with an Al Kα X-ray source.

For the Ru@MXene and Ru@P-MXene samples, a JEOL JEM-ARM200F transmission electron microscope operated in scanning transmission electron microscopy (STEM) mode at 200 kV accelerating voltage was used to analyze the Ru morphologies *via* high-angle annular dark field (HAADF-STEM) imaging. The samples were prepared by dispersing the catalyst powders in ethanol, followed by 30 min of sonication. The resulting suspension was drop-cast onto lacey carbon grids and dried prior to imaging. Elemental mapping was performed using energy-dispersive X-ray spectroscopy (EDS) with an Oxford XMAX TLE 100 mm^2 windowless EDS detector integrated with an ARM200F microscope.

2.4 Catalytic hydrogenolysis tests

Hydrogenolysis of LDPE was conducted in a 50 mL stainless steel Parr batch reactor following a reported procedure.[24] A total of 0.1 g of the reduced Ru@MXene or Ru@P-MXene catalyst and 2.0 g of LDPE (feed-to-catalyst ratio of 20 : 1) were added to the reactor. The reactor was then sealed, purged 5 times with H_2 at 15 bar, and subsequently pressurized to 30 bar H_2 at room temperature (∼20 °C). The reactor was placed on a heating stirrer set to 500 rpm and heated to 250 °C. The gaseous products (C_1–C_4) were collected in a 1 L Tedlar gas sampling bag and analyzed using a GC-FID (Agilent CP-Volamine GC column). The residual content in the reactor was treated with ∼20 mL of methylene chloride (CH_2Cl_2, HPLC grade, ≥99.9%) containing 20 mg of *n*-octacosane ($C_{28}H_{58}$, ≥98.0%) as an external standard. After filtration, the soluble fraction was defined as the liquid products (C_5–C_{35}), while the unreacted polymer retained on the filter paper was classified as a solid residue (>C_{35}). The liquid products were analyzed by GC-FID (Agilent HP-1 column) and identified by GC-MS (Agilent DB-1 column). Product yields for both gas and liquid phases were calculated on a molar basis. Polymer conversion was determined gravimetrically, based on the mass difference between the initial amount of the polymer added and the unreacted residue collected on the filter paper.

3. Results and discussion

3.1 Transition from the liquid phase to vapor-phase pillarization of MXene

Silica-pillared MXene has previously been synthesized through liquid-phase processing, which requires large amounts of solvent and multiple operational steps. One report from Bimbo's group[11] involved co-intercalation of DDA and TEOS, followed by hydrolysis in water. In this work, MXene was dispersed in a solution of DDA dissolved in TEOS under an argon (Ar) atmosphere at room temperature, with a typical molar ratio of MXene/DDA/TEOS = 1 : 6–10 : 15–20. After filtration and drying, the intercalated MXene was dispersed in water at a MXene/water mass ratio of 1 : 50. After drying, the sample at this stage exhibited a surface area of 235 $m^2\ g^{-1}$ and a pore size of ∼10 Å. The sample was then calcined in Ar at 400 °C to remove trapped DDA while preserving the pillared structure. The surface area was reduced to 141 $m^2\ g^{-1}$ with a pore size of ∼32 Å after calcination. The other study, by Pérez-Carvajal's group,[40] reported a synthesis process involving intercalation, hydrolysis, and extraction steps. First, MXene was dispersed in a cetyltrimethylammonium bromide (CTAB) solution at a mass ratio of MXene/CTAB/water = 1 : 0.25 : 200. After drying, the CTAB-intercalated MXene was redispersed in isopropanol, followed by the addition of tetramethyl orthosilicate (TMOS) for intercalation and a water/methanol mixture for TMOS hydrolysis (molar ratio MXene/TMOS/water/methanol = 1 : 1 : 2 : 2). After centrifugation and drying, CTAB was removed from the sample using a hydrochloric acid/ethanol solution at 70 °C. The final dried material exhibited a surface area of 290 $m^2\ g^{-1}$ with an average pore width of ∼120 Å.

Building on these prior liquid-phase pillaring protocols, we developed a vapor-phase operation route that reduces solvent use, minimizes operational steps, and generates less liquid waste for the synthesis of silica-pillared MXene. Our reagents mirror those in the LPP method reported by Bimbo's group:[11] DDA as the swelling agent, TEOS as the intercalation precursor, and water for hydrolysis. DDA, a linear alkyl amine with a terminal $-NH_2$ group, forms hydrogen bonds with –OH terminations on MXene, expanding the interlayer spacing and facilitating TEOS intercalation.[9] Compared with cationic surfactants of similar chain length (*e.g.*, CTAB[41]), DDA induces a greater expansion of interlayer spacing, which is attributed to the formation of a bilayer structure with vertically aligned orientation relative to the 2D nanosheets.[42,43] As a basic amine, DDA also catalyzes TEOS hydrolysis in humid environments. To prevent premature interaction between DDA and TEOS before diffusion into MXene, we co-located DDA and MXene in a container while keeping TEOS in a separate compartment (Scheme 1). Because DDA melts at ∼27–31 °C but boils near 247–249 °C, we selected an intercalation temperature between its melting and boiling points (*e.g.*, 100 °C) to limit volatilization. Upon heating, the molten DDA is drawn into the MXene galleries by capillary forces. TEOS boils near 168–170 °C, so operating below its boiling point slows undesired hydrolysis with exterior –OH groups on MXene and allows deeper penetration into the galleries. Hydrolysis was then carried out in the same setup by replacing the TEOS source with water and lowering the temperature to 80 °C.

Guided by liquid-phase pillarization compositions,[9] we tested two VPP regimes: (i) DDA loading comparable to the liquid-phase process with reduced TEOS (*e.g.*, a mass ratio of MXene/DDA/TEOS = 1 : 5–20 : 0.1–1), and (ii) TEOS loading comparable to the liquid-phase process with reduced DDA (*e.g.*, a mass ratio of MXene/DDA/TEOS = 1 : 0.8 : 1.6–20). These experiments defined practical reagent windows for producing silica-pillared MXene while substantially lowering overall reagent consumption. For comparison, we also conducted two trials without DDA and with a MXene/DDA ratio of 10, but with DDA placed together with TEOS, both staying outside the MXene compartment. In the absence of DDA, the N_2 isotherm of the product closely matched that of pristine MXene (Fig. S1, SI), indicating minimal interlayer expansion and limited TEOS access. When DDA was added to the TEOS compartment, its high boiling point hindered effective evaporation and diffusion into the MXene galleries, yielding only a slight increase in N_2 uptake (Fig. S1, SI). Collectively, these results suggest that the identified VPP conditions are optimal for synthesizing mesoporous P-MXene.

Table 1 Atomic compositions for MAX, MXene, and P-MXene measured by EDX

	Atomic composition (%)						
Materials	C	Al	Ti	O	F	Cl	Si
MAX	24.5	22.6	39.0	13.8	—	—	—
MXene	20.1	0.4	30.0	30.9	16.8	1.8	—
P-MXene[a]	20.7	0.3	22.5	48.5	5.2	0.6	2.2
P-MXene[b]	16.3	0.2	22.6	47.6	8.0	0.3	5.1

[a] Synthesis conditions: VPP, MXene/DDA/TEOS/H_2O = 1 : 10 : 0.5 : 10 (mass ratio), intercalation at 100 °C, and hydrolysis at 80 °C. [b] Synthesis conditions: VPP, MXene/DDA/TEOS/H_2O = 1 : 0.8 : 6.4 : 10 (mass ratio), intercalation at 100 °C, and hydrolysis at 80 °C.

3.2 Verification of VPP effectiveness in synthesizing silica-pillared MXene

To evaluate the effectiveness of the VPP process for synthesizing silica-pillared MXene, we first used an intercalation mass ratio of MXene/DDA/TEOS = 1 : 10 : 0.5. Assuming a MXene composition of Ti_3C_2–OH, the corresponding molar ratio of MXene/DDA/TEOS is 1 : 10 : 0.9. In the subsequent hydrolysis step, the MXene/H_2O mass ratio was 1 : 10, equivalent to a molar ratio of 1 : 103. Intercalation was carried out at 100 °C for 24 h, followed by hydrolysis at 80 °C for 24 h. The resulting material was then calcined under a N_2 atmosphere at 400 °C for 12 h. These conditions were defined as the baseline for further investigating the effects of VPP parameters on the synthesis of silica-pillared MXene, as discussed in Section 3.3 below.

The elemental compositions of MXene and P-MXene were analyzed using energy-dispersive X-ray spectroscopy (EDX) measurements, with the parent MAX phase included for comparison. The MAX shows a stoichiometry of $Ti_{1.6}C_{1.0}Al_{0.9}O_{0.6}$. In the etched MXene, Al atomic composition was reduced to 0.4%, confirming successful removal of Al layers (Table 1). The MXene composition is $Ti_{1.5}C_{1.0}Al_{0.02}O_{1.5}X_{0.9}$ (X stands for F and Cl) from the EDX data. The slightly lower Ti/C ratio relative to MAX suggests that minor Ti dissolution during etching, and the presence of F and Cl, and increased O content indicates the formation of surface terminations. After vapor-phase

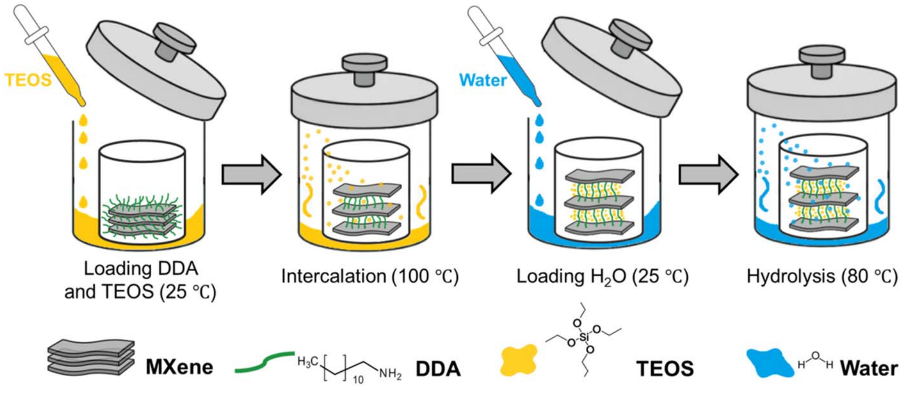

Scheme 1 Schematic of vapor phase pillarization (VPP) of MXene into P-MXene.

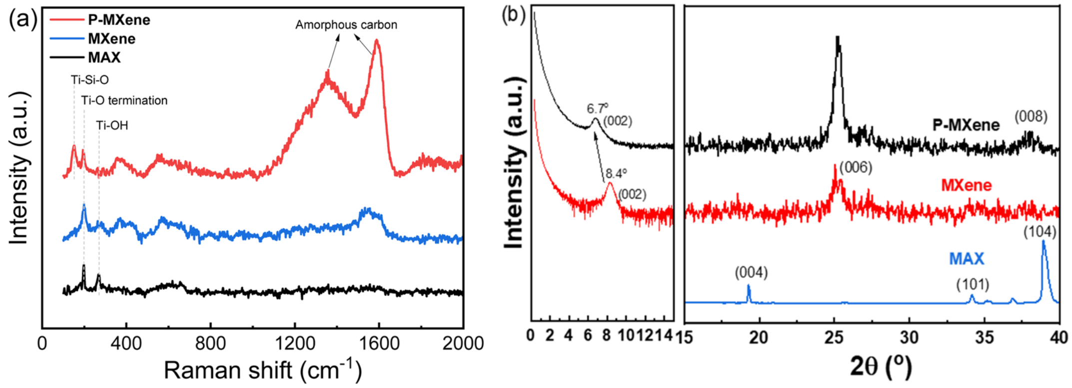

Fig. 1 (a) Raman and (b) XRD data of MAX, MXene and P-MXene materials. (P-MXene synthesis conditions: MXene/DDA/TEOS/H_2O = 1 : 10 : 0.5 : 10 (mass ratio), intercalation at 100 °C, and hydrolysis at 80 °C).

pillarization, P-MXene exhibits a composition of $Ti_{1.1}C_{1.0}Al_{0.01}O_{2.3}X_{0.3}Si_{0.1}$, which means Ti and C were largely retained, while the increases in O and Si confirm successful incorporation of silica pillars. The reduced X content points to partial loss of F/Cl terminations during VPP. No nitrogen (N) signal was observed, consistent with removal of DDA during calcination.

Because EDX is insensitive to hydrogen, we used Raman spectroscopy to probe –OH and/or –O surface terminations in MXene and P-MXene (Fig. 1a). The MAX precursor shows a sharp band at ~198 cm^{-1} (Ti–O) and a weaker band at ~270 cm^{-1}(Ti–OH).[9] Both features persist in the etched MXene phase. After VPP, P-MXene retains the ~198 cm^{-1} band, whereas the ~270 cm^{-1} band disappears, consistent with consumption of Ti–OH groups during silica pillar formation. A new band at ~152 cm^{-1} can be assigned to the Ti–Si–O linkage[44] formed during VPP. Additional bands below 1000 cm^{-1} are attributable to overlapping Ti–X vibrations (X = F, Cl).[45] The broad band at 1200–1700 cm^{-1} in both MXene and P-MXene indicates the presence of amorphous carbon, likely due to slight over-etching of the MAX precursor.[11]

X-ray diffraction patterns (Fig. 1b) were used to analyze the crystal structures of MXene and P-MXene. MXene exhibits characteristic reflections at 2θ ~8.4°, 25.3°, and 38.0°, indexed to the (002), (006), and (008) planes, respectively.[46] No diffraction peaks from the parent MAX phase are observed, which indicates successful etching of the MXene phase. Notably, the (002) peak shifts from 2θ ~9.5° (MAX) to 8.4° (MXene), evidencing an increased interlayer spacing per Bragg's law. From the (002) reflection, the calculated *d*-spacing in MXene is ~1.1 nm. The average interlayer spacing can be estimated by subtracting the layer thickness (*i.e.*, 0.9 nm, obtained from the TEM result discussed below) from the *d*-spacing, yielding ~0.2 nm. After VPP, the (002) peak further shifts to 2θ ~6.7°, corresponding to a *d*-spacing of ~1.3 nm and a gallery height of ~0.4 nm. This trend agrees with previous reports on MXene pillarization *via* the LPP approach.[8,9]

The morphology of MXene and P-MXene was characterized using SEM and TEM imaging. The parent MAX phase exhibits a compact, densely layered structure (Fig. S2 in the SI). After selective Al etching, the resulting MXene displays thin, flexible, sheet-like morphologies with curled edges (Fig. 2a). Following VPP pillarization, P-MXene retained its sheet-like architecture. However, the sheets appear narrower, thicker, and with straighter edges (Fig. 2b). TEM images further resolve the internal stacking. MXene shows multiple stacked layers with an individual layer thickness of ~0.90 nm and an interlayer spacing of ~0.25 nm (Fig. 2c), in good agreement with the XRD-derived gallery height (Fig. 1b). After VPP, the interlayer spacing of P-MXene increased substantially to ~5–20 nm, while the single-layer thickness remained ~0.90 nm (Fig. 2d). Silica pillar particles (highlighted by green circles) are clearly visible within the galleries of P-MXene. The broad distribution of interlayer distances indicates that pillars form non-uniformly between adjacent MXene nanosheets.

N_2 adsorption–desorption isotherms were used to evaluate the textural properties of MXene and P-MXene. As shown in Fig. 3a, MXene exhibits very limited N_2 uptake across the entire relative pressure range. A closer look at Fig. 3a indicates a type II

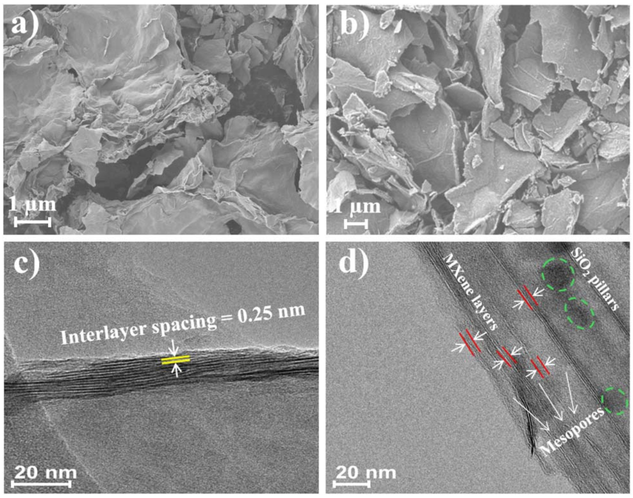

Fig. 2 SEM images of MXene (a) and P-MXene (b), and TEM images of MXene (c) and P-MXene (d). The regions highlighted with green dashed circles in (d) indicate the presence of silica pillars (P-MXene synthesis conditions: MXene/DDA/TEOS/H_2O = 1 : 10 : 0.5 : 10 (mass ratio), intercalation at 100 °C, and hydrolysis at 80 °C).

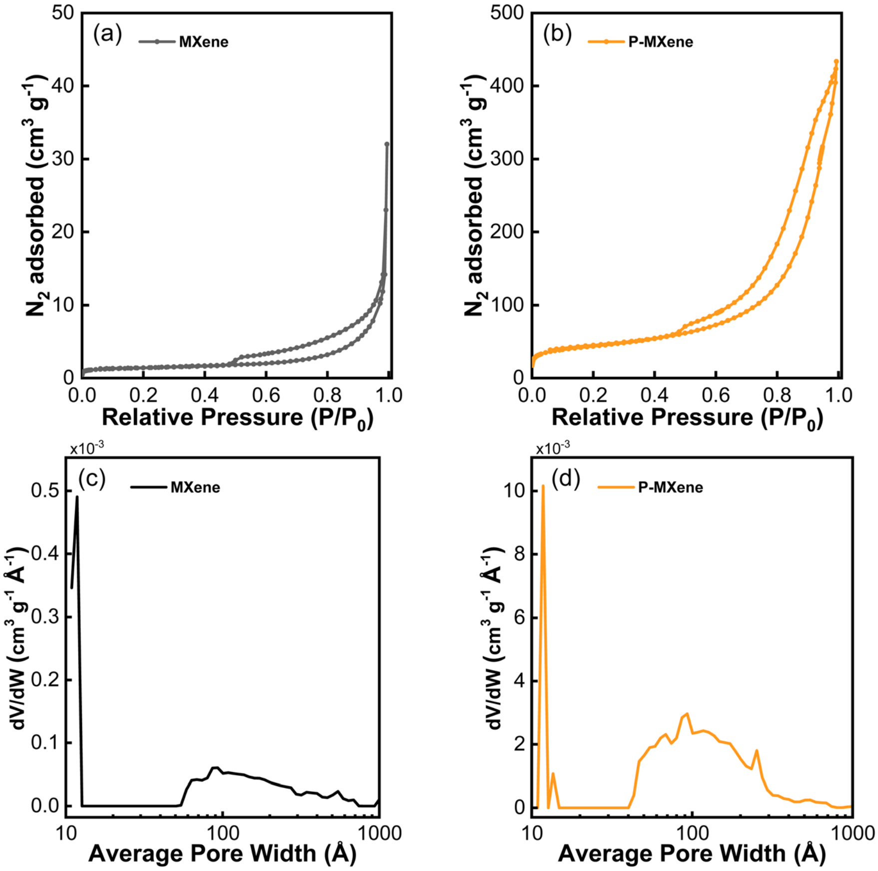

Fig. 3 N_2 adsorption–desorption isotherms (a and b) and the corresponding pore size distributions (c and d) of MXene and P-MXene materials. (P-MXene synthesis conditions: MXene/DDA/TEOS/H_2O = 1 : 10 : 0.5 : 10 (mass ratio), intercalation at 100 °C, and hydrolysis at 80 °C).

isotherm with an H3-type hysteresis loop, according to IUPAC classification.[47,48] The hysteresis loop is characteristic of a plate-like layered structure that contains wedge-shaped pores among stacked MXene nanosheets. Overall, MXene displays a low total pore volume (0.014 $cm^3\ g^{-1}$) and a low BET surface area (4 $m^2\ g^{-1}$), as corroborated by the pore size distribution (Fig. 3c) and cumulative pore volume data (Table S1). In contrast, P-MXene displays markedly higher N_2 uptake across the full relative pressure range (Fig. 3b). The adsorption isotherm increases progressively at low relative pressures ($P/P_0 < 0.48$), consistent with micropore filling. The pronounced hysteresis at $0.48 < P/P_0 < 1.00$ arises from capillary condensation in mesopores. The persistence of the loop approaching $P/P_0 \sim 1.00$ suggests the presence of macropores as well. The isotherm is also type II with an H_3 hysteresis loop, indicative of existence of wedge-shaped mesopores,[47,48] but the amount of these pores increased significantly than that in the MXene sample. The pore size distribution and cumulative pore volume data (Fig. 3d and Table S1) confirm a hierarchy of micro-, meso-, and macropores in P-MXene, with dominant pore widths in the mesopore range (~5–35 nm), consistent with TEM observations (Fig. 2d). The cumulative pore volume increases dramatically to 0.53 $cm^3\ g^{-1}$, and the BET surface area increases to 148 $m^2\ g^{-1}$ for P-MXene. Notably, this improvement approaches that of SiO_2-pillared MXene prepared by the LPP method in the literature[9] (~141 $m^2\ g^{-1}$ from an initial 4 $m^2\ g^{-1}$), despite using only ~2.5% of the TEOS amount (MXene/TEOS = 1 : 0.5 in VPP *vs.* 1 : 20 in LPP). This demonstrates the efficiency of VPP in boosting the surface area of MXene materials while minimizing precursor consumption and TEOS-related waste.

3.3 Vapor-phase pillarization of MXene under high DDA and low TEOS conditions

Beginning with the base composition (mass ratio of MXene : DDA : TEOS : H_2O = 1 : 10 : 0.5 : 10) in the VPP, we systematically varied the amount of DDA, the quantity of TEOS, the water content during the hydrolysis step, and the type of the swelling agent (*e.g.*, HA and ODA) to examine their influences on the formation of P-MXene. We employed N_2 adsorption–desorption isotherms to quantify the BET surface area, pore volume, pore-size distributions, and pore geometry, and used these data to compare the samples and correlate textural characteristics with synthesis conditions, thereby establishing processing–structure relationships to engineer interlayer mesopores in MXene pillarization.

We first varied the DDA amount during the VPP intercalation step by adjusting the DDA/MXene mass ratio from the base case (*i.e.*, 10) to 5 and 20. The absence of DDA (*i.e.*, DDA/MXene = 0) in the synthesis was included for comparison. The corresponding N_2 adsorption–desorption isotherms are shown in

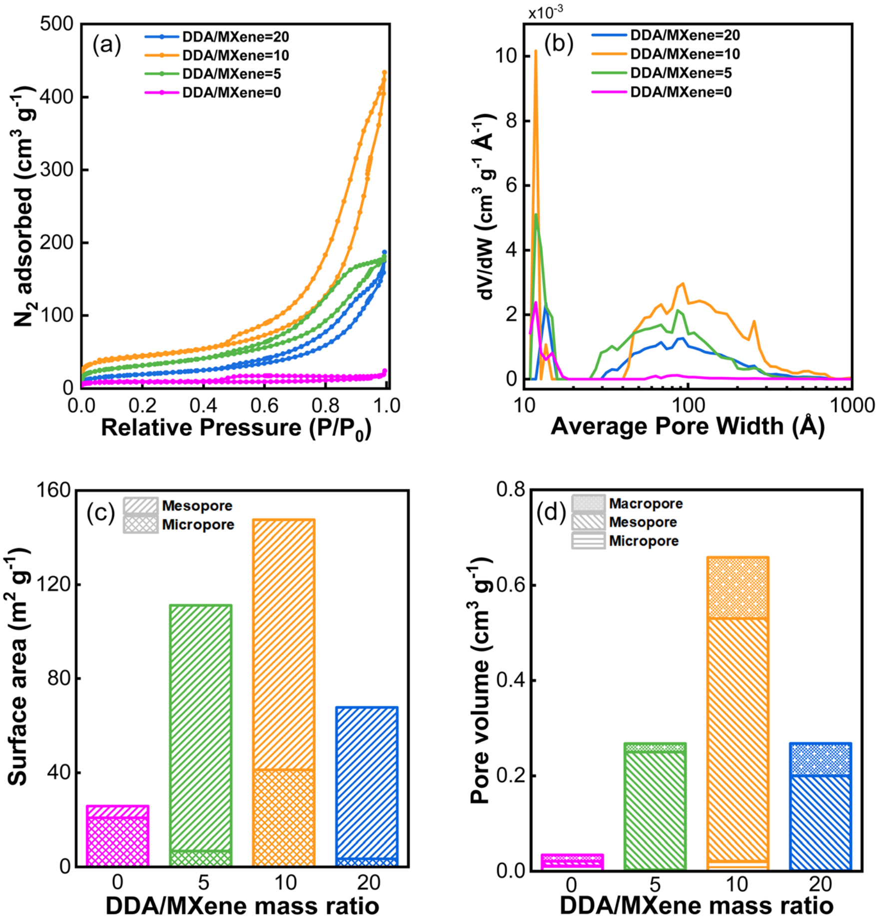

Fig. 4 Textural properties of P-MXene prepared by VPP as a function of DDA loading during intercalation. (a) N_2 adsorption–desorption isotherms; (b) pore-size distributions; (c) surface area partitioned into micro- and meso-contributions; (d) corresponding micro-, meso-, and macropore volumes. The samples were synthesized at DDA : MXene mass ratios of 0, 5, 10, and 20. (Synthesis conditions: MXene/TEOS/H_2O = 1 : 0.5 : 10 (mass ratio), intercalation at 100 °C, and hydrolysis at 80 °C).

Fig. 4a. As the ratio increased from 5 to 10, the overall N_2 uptake rose, but it decreased at a ratio of 20. In all three cases (5, 10, and 20), the resultant P-MXene samples exhibit higher N_2 uptake than pristine MXene across the micropore ($P/P_0 < 0.50$), mesopore ($0.50 < P/P_0 < 0.98$), and macropore ($P/P_0 > 0.98$) regions. At a ratio of 5, the isotherm is type IV with an H2b hysteresis loop, indicative of ink-bottle-type mesopores with a broad distribution of neck sizes. At a mass ratio of 10, the isotherm is type II with an H3 hysteresis loop, characteristic of wedge- or slit-shaped pores in layered materials. An abrupt closure of the desorption branch onto the adsorption branch is observed in the mesopore region at $P/P_0 = 0.5$, consistent with cavitation. At a ratio of 20, the mesopore features resemble those at a ratio of 5, but with more pronounced macroporosity, as evidenced by the increased uptake at $P/P_0 > 0.98$. The BET surface area follows a volcano-type trend with DDA usage (Fig. 4c and Table S2), as do the meso- and macro-pore volumes (Fig. 4d and Table S2). The mesopore-size distributions (Fig. 4b) show that P-MXene prepared at DDA : MXene mass ratios of 5, 10, and 20 exhibit pore ranges of 25–350 Å, 40–450 Å, and 30–400 Å, respectively. The ratio of 10 yields a pronounced increase in pores between 100 and 300 Å compared with the other samples. Collectively, these results indicate interconnected micro-, meso-, and macroporosity in all resultant P-MXene materials, with DDA playing a critical role in tuning texture. We hypothesize that at low DDA loadings, DDA intercalates with a bias toward the stack perimeter, expanding only the edge-adjacent galleries of the MXene bilayer. TEOS vapor is then confined to these regions and, upon hydrolysis/condensation, forms silica pillars that create narrow necks (ink-bottle mesopores). With higher DDA (DDA : MXene = 10), the layers expand more toward the interior of the stack, allowing TEOS to infiltrate the galleries and generate wedge/slit-shaped pores. At excessive DDA (DDA : MXene = 20), the galleries become overfilled with DDA, preventing TEOS from penetrating beyond the edges. Upon calcination, the DDA escapes and the nanosheets partially collapse, yielding only limited increases in surface area and pore volume.

Furthermore, the effects of DDA intercalation time were studied by conducting a control experiment with an extension of the VPP duration from 24 h to 48 h under otherwise identical synthesis conditions (MXene/DDA/TEOS/H_2O = 1 : 5 : 0.5 : 10 by mass; intercalation at 100 °C and hydrolysis at 80 °C). Fig. S3 shows that prolonging the VPP time does not significantly alter the overall textural properties. The N_2 adsorption–desorption isotherms in the micro- and mesopore regions remain nearly unchanged, indicating that the corresponding pore structures are largely preserved. However, extending the treatment to 48 h results in a noticeable increase in macroporosity. This increase may arise from further accumulation of DDA and TEOS near the edge regions of the MXene galleries, where precursor access is less diffusion-limited. These results suggest that longer reaction times primarily promote macropore development through continued deposition or aggregation of pillaring species at the sheet perimeters, while the micro- and mesoporous structures remain essentially intact. This behavior likely reflects saturation of the swelling agent and silica precursor within the confined interior galleries after an initial equilibration period.

We next examined the effect of TEOS loading during intercalation by varying the TEOS : MXene mass ratio from the base conditions of 0.5 to 0.1, 1.0 and 20. As shown in Fig. 5a, all samples display type II isotherms with an H3 hysteresis loop, indicative of wedge/slit-shaped mesopores. The BET surface area increases as the TEOS : MXene ratio increases from 0.1 to 0.5, and then decreases at 1.0 and 20.0 (Fig. 5c and Table S3)). The meso- and total pore volumes follow the same trend (Fig. 5d and Table S3). The hysteresis loops in the mesopore range ($0.5 < P/P_0 < 0.98$) grow substantially, particularly at $0.8 < P/P_0 < 0.98$, when the ratio increases from 0.1 to 0.5, and diminish at higher TEOS loadings, with a pronounced reduction at $0.5 < P/P_0 < 0.8$, consistent with fewer smaller mesopores. The mesopore size distributions (Fig. 5b) span ∼20–250 Å at a ratio of 0.1 with a prominent feature near ∼100 Å; they broaden to ∼40–300 Å at 0.5, and narrow slightly to ∼55–300 Å at 1.0 with a much weaker peak than at 0.5. We attribute the low surface area/porosity at low TEOS loading to an insufficient number of silica pillars, while the decrease at high loading likely arises from overfilling of the interlayer galleries by excess silica, causing densification and reduced accessible porosity. Notably, a TEOS : MXene ratio of 20 approximates that used in the LPP method,[11] yet the surface area achieved by VPP under these conditions (33 $m^2\ g^{-1}$) is far lower than that reported for LPP (141 $m^2\ g^{-1}$). In LPP, excess TEOS is removed by filtration prior to calcination, a step not implemented in VPP. Overall, these results indicate that P-MXene formation *via* VPP requires reagent compositions distinct from those effective in LPP.

We evaluated the effect of water during the VPP hydrolysis step by varying the water : MXene mass ratio from 10 in the base conditions to 0 and 20. As shown in Fig. 6a, omission of added water (ratio = 0) still yields higher N_2 uptake than pristine

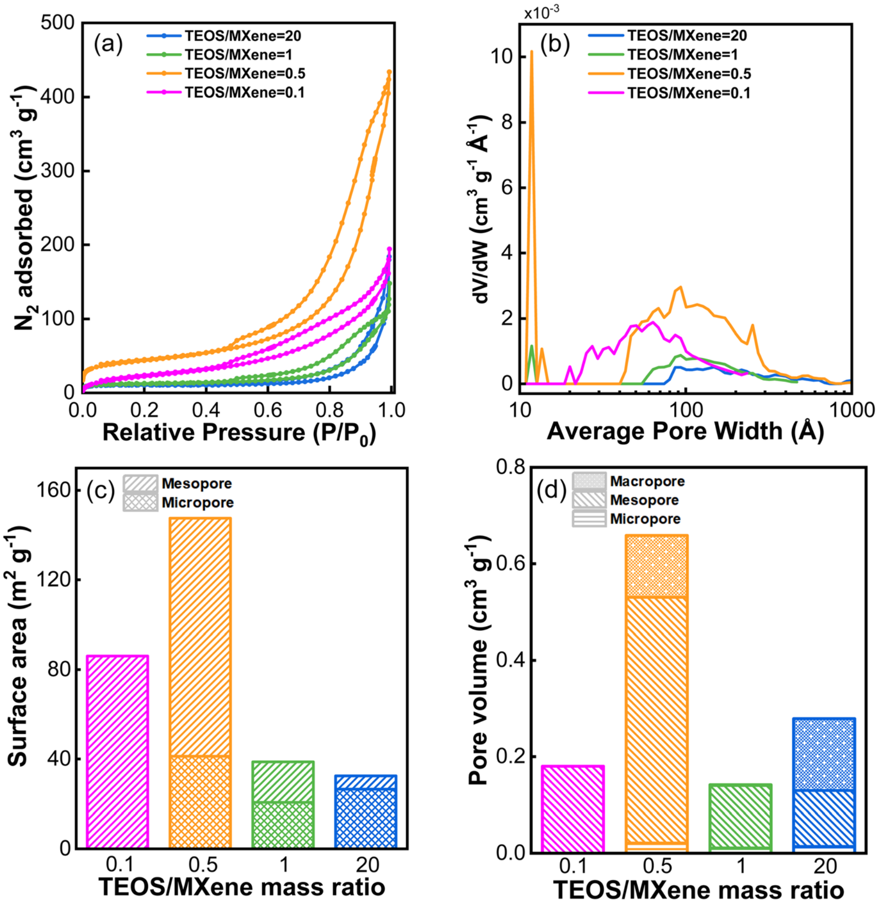

Fig. 5 Textural properties of P-MXene prepared by VPP as a function of TEOS loading during intercalation. (a) N_2 adsorption–desorption isotherms; (b) pore-size distributions; (c) surface area partitioned into micro- and meso-contributions; (d) corresponding micro-, meso- and macropore volumes. The samples were synthesized at TEOS : MXene mass ratios of 0.1, 0.5, 1, and 20. (Synthesis conditions: MXene/DDA/H_2O = 1 : 10 : 10 (mass ratio), intercalation at 100 °C, and hydrolysis at 80 °C).

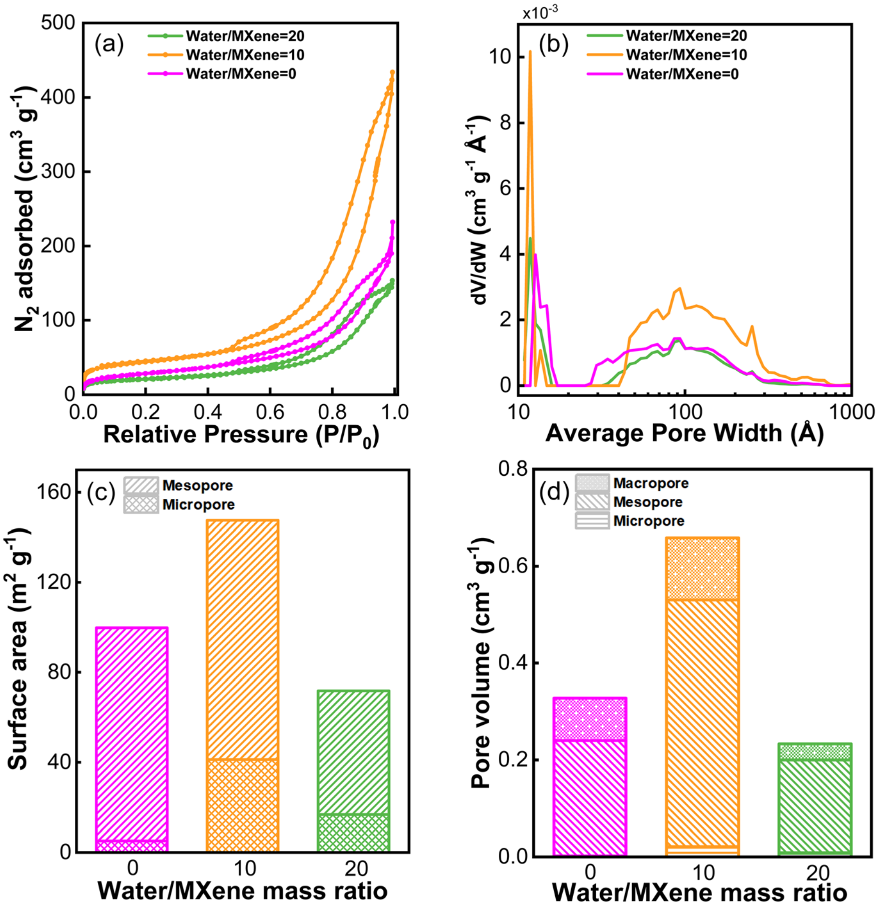

Fig. 6 Textural properties of P-MXene prepared by VPP as a function of water loading during hydrolysis. (a) N_2 adsorption–desorption isotherms; (b) pore-size distributions; (c) surface area partitioned into micro- and meso-contributions; (d) corresponding micro-, meso- and macropore volumes. The samples were synthesized at water : MXene mass ratios of 0, 10, and 20. (Synthesis conditions: MXene/TEOS/DDA = 1 : 0.5 : 10 (mass ratio), intercalation at 100 °C, and hydrolysis at 80 °C).

MXene, though lower than that obtained at a ratio of 10. The isotherm at a ratio of 0 is type IV with an H2b hysteresis loop and a sharp uptake at $P/P_0 > 0.98$ indicates the presence of macropores. At a ratio of 20, the overall N_2 uptake decreases below even the no-water case, and the high-pressure uptake ($P/P_0 > 0.98$) is no longer prominent, while the isotherm remains type IV with H2b hysteresis. Across the tested water : MXene ratios, the BET surface area increases from 0 to 10 and then decreases at 20 (Fig. 6c and Table S4). The mesopore and total pore volumes follow the same trend (Fig. 6d and Table S4). The mesopore size distributions (Fig. 6b) show that the no-water sample (ratio = 0) favors smaller pores (~25–300 Å) compared with the ratio-of-10 sample (~40–450 Å). At a ratio of 20, the distribution range resembles that at 10 but with uniformly lower intensity. In the presence of water, intercalated TEOS is converted to silica *via* hydrolysis ($Si(OCH_2CH_3)_4 + 4H_2O \rightarrow Si(OH)_4 + 4C_2H_5OH$) and condensation ($Si(OH)_4 \rightarrow SiO_2 + 2H_2O$) reactions. Assuming TEOS does not react with terminal –OH groups on MXene, the stoichiometric water requirement corresponds to a mass ratio of MXene/TEOS/DDA/H_2O = 1 : 0.5 : 10 : 0.09. This means ~9 wt% water relative to MXene mass is sufficient for complete TEOS hydrolysis. TGA indicates ~2 wt% water in the as-prepared MXene (Fig. S4 in the SI), explaining why some pillarization occurs even without added water. The decline in N_2 uptake at higher water content is plausibly due to disruption of the DDA bilayer between MXene sheets: strong H_2O–amine interactions can destabilize the bilayer and weaken hydrogen bonding with MXene–OH groups, thereby reducing VPP pillaring efficiency.

As a swelling agent, DDA comprises a linear C_{12} hydrocarbon chain terminating in an $-NH_2$ group ($CH_3-(CH_2)_{11}-NH_2$). Because amines of different hydrocarbon chain lengths are available, we hypothesized that the chain length, and thus the molecular size, would affect both interlayer expansion and pillarization efficiency. To probe this, we replaced DDA with hexylamine (HA, $CH_3-(CH_2)_5-NH_2$) and octadecylamine (ODA, $CH_3-(CH_2)_{17}-NH_2$) at equal molar loadings in the VPP process, enabling a direct comparison of chain-length effects. The N_2 adsorption–desorption isotherms (Fig. 7a) show lower overall uptakes for HA- and ODA-derived samples than for DDA. When HA is used, the isotherm exhibits features of a type IV curve with an H2b hysteresis loop beginning near $P/P_0 = 0.6$ and a pronounced high-pressure uptake ($P/P_0 > 0.98$), indicative of macroporosity. For ODA, the isotherm displays a clearer type IV

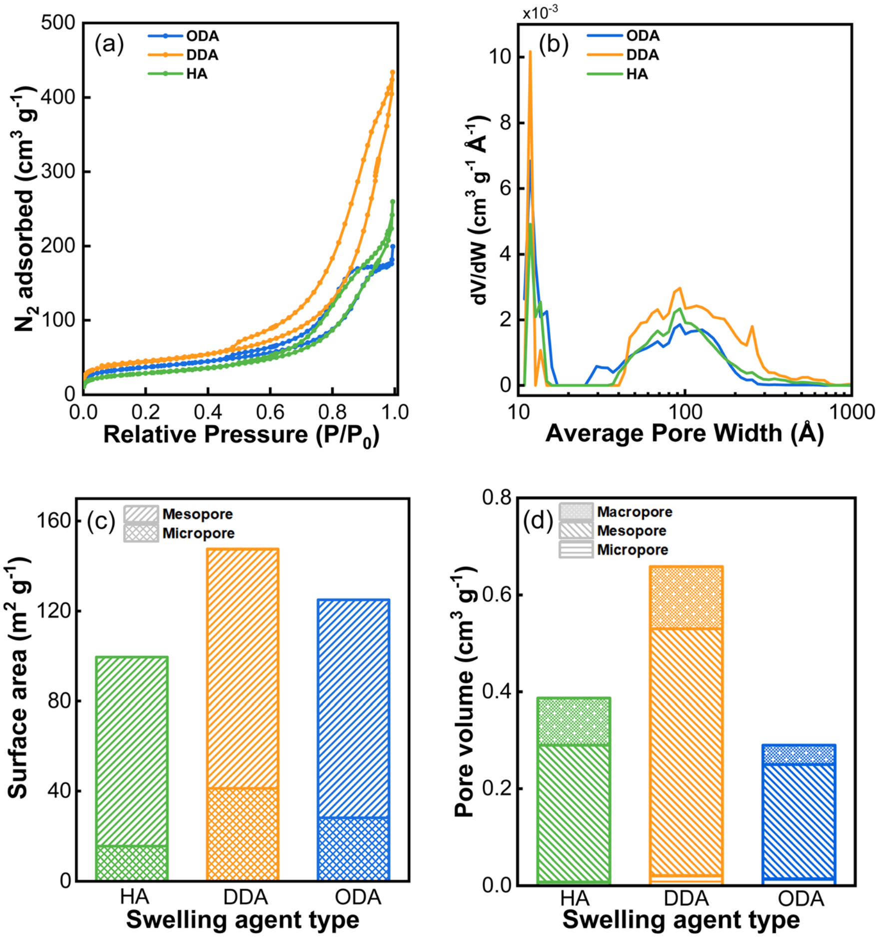

Fig. 7 Textural properties of P-MXene prepared by VPP with different swelling agents (HA, DDA, or ODA) during intercalation. (a) N_2 adsorption–desorption isotherms; (b) pore-size distributions; (c) surface area partitioned into micro- and meso-contributions; (d) corresponding micro-, meso-, and macropore volumes. (Synthesis conditions: MXene/DDA/TEOS/H_2O = 1 : 10 : 0.5 : 10 (mass ratio), intercalation at 100 °C, and hydrolysis at 80 °C; for HA and ODA, the molar numbers were controlled to be the same as DDA).

profile with an H2b loop, consistent with ink-bottle-type mesopores. Macropore-related uptake at $P/P_0 > 0.98$ is also evident. The BET surface area increases from HA to DDA, and then decreases with ODA (Fig. 7c and Table S5). The meso- and total pore volumes follow the same trend (Fig. 7d and Table S5). Pore-size distributions (Fig. 7b) shift to smaller characteristic sizes for both HA and ODA relative to DDA. These results suggest that HA is too short to substantially expand the MXene interlayer galleries, while ODA, although capable of promoting expansion, occupies excessive volume and limits TEOS access, suppressing pore development. By contrast, the intermediate chain length of DDA provides a more favorable balance, facilitating interlayer expansion and TEOS diffusion into interior regions, thereby enhancing formation of well-pillared structures.

3.4 Vapor-phase pillarization of MXene under low DDA and high TEOS conditions

We hypothesized that a DDA : MXene mass ratio of 10 preoccupies the interlayer galleries with DDA, impeding TEOS intercalation and thus limiting the formation of highly porous P-MXene. To test this, we conducted a second set of VPP experiments using a lower DDA : MXene ratio (0.8) while increasing TEOS loading. All other conditions matched the base case. Specifically, the TEOS : MXene mass ratio was varied stepwise to 1.6, 3.2, 6.4, 10.0, and 20.0. The N_2 adsorption–desorption isotherms for the P-MXene samples prepared under these conditions are shown in Fig. 8a. All exhibit type IV isotherms with H2b hysteresis and a pronounced high-pressure uptake at $P/P_0 > 0.98$, indicating macroporosity. This behavior contrasts with the first VPP set (higher DDA), which showed more restricted-neck mesoporosity. At lower TEOS loadings (TEOS : MXene = 1.6), the micropore uptakes are comparable, and capillary condensation onsets near $P/P_0 \sim 0.60$. Increasing the TEOS loading (TEOS : MXene = 6.4) produces a clear rise in mesopore and macropore uptake. At still higher TEOS loadings (*e.g.*, TEOS : MXene = 10 and 20), both micropore and mesopore uptakes increase further, and the condensation onset shifts to lower relative pressure ($P/P_0 \sim 0.42$), consistent with the formation of small-width mesopores.

The surface area increases monotonically with TEOS loading, and all samples surpass those from the first VPP set

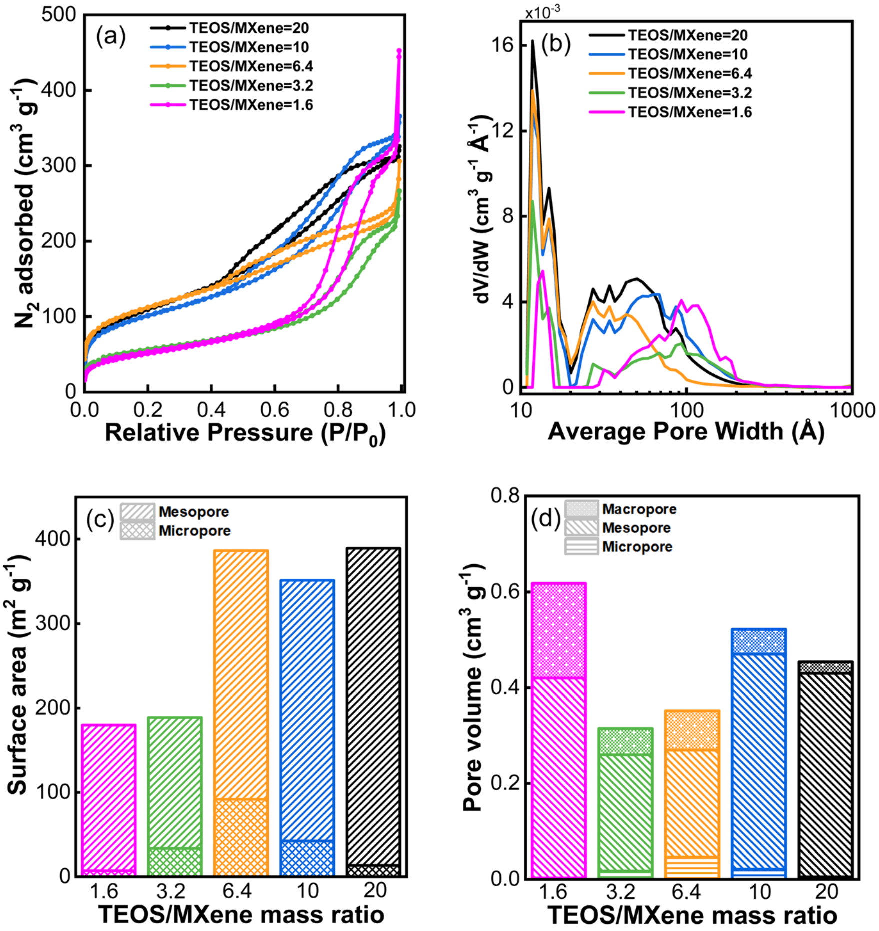

Fig. 8 Textural properties of P-MXene prepared by VPP as a function of TEOS loading during intercalation. (a) N_2 adsorption–desorption isotherms; (b) pore-size distributions; (c) surface area partitioned into micro- and meso-contributions; (d) corresponding micro-, meso-, and macropore volumes. The samples were synthesized at TEOS : MXene mass ratios of 1.6, 3.2, 6.4, 10, and 20. (Synthesis conditions: MXene/DDA/H_2O = 1 : 0.8 : 10 (mass ratio), intercalation at 100 °C, and hydrolysis at 80 °C).

(Fig. 8c and Table S6). Notably, the TEOS : MXene = 6.4 sample reaches 386 m^2 g^{-1}, more than twice the value reported for liquid-phase pillaring. The total pore volume (Fig. 8d and Table S6) shows a non-monotonic trend: it decreases at intermediate TEOS and then increases again at higher TEOS, suggesting that partial occupation of the interlayer galleries by TEOS initially reduces accessible volume, while greater TEOS ultimately enhances pillar formation and restores porosity. The pore-size distributions (Fig. 8b) shift toward smaller mesopore widths at higher TEOS loadings, in agreement with the lower condensation onset. Overall, these results imply that a small amount of DDA is sufficient to swell the MXene layers, creating interlayer space for TEOS intercalation and pillar growth, thereby strengthening the pillaring effect.

Using the optimized composition (MXene : DDA : TEOS = 1.0 : 0.8 : 6.4), we next examined the effect of intercalation temperature. This was motivated by the observation that a substantial fraction of TEOS remained unreacted in the external reservoir when intercalation proceeded at the base temperature. Accordingly, intercalation was conducted at 80, 130, and 170 °C, and the resulting VPP-pillared MXene samples were characterized by N_2 adsorption–desorption. As shown in Fig. 9a, mesoporosity is retained at the higher temperatures (130 and 170 °C), but the BET surface areas decrease to 310 and 257 m^2 g^{-1}, respectively (Fig. 9c and Table S7). At 80 °C, the BET surface area also declines to 309 m^2 g^{-1}. A yellow coloration observed after high-temperature intercalation is consistent with partial DDA decomposition, which would reduce swelling efficacy and hinder TEOS penetration into the galleries. At the lower temperature, reduced TEOS delivery to the interlayer space likely limits pillar formation. Consequently, pillaring performance is compromised at both ends of the temperature range. Notably, the pore volumes (Fig. 9d and Table S7) and the pore size distribution trends (Fig. 9b) fluctuate with temperature, indicating a more complex temperature dependence.

3.5 Mechanistic understanding of hierarchical porosity structure formation

With an improved understanding of the structure–property evolution of the resultant P-MXene materials under different VPP conditions, we propose a mechanistic model for the development of hierarchical porosity in silica-pillared MXene. The synthesis begins with freeze drying of delaminated MXene sheets dispersed in suspension, during which partial restacking

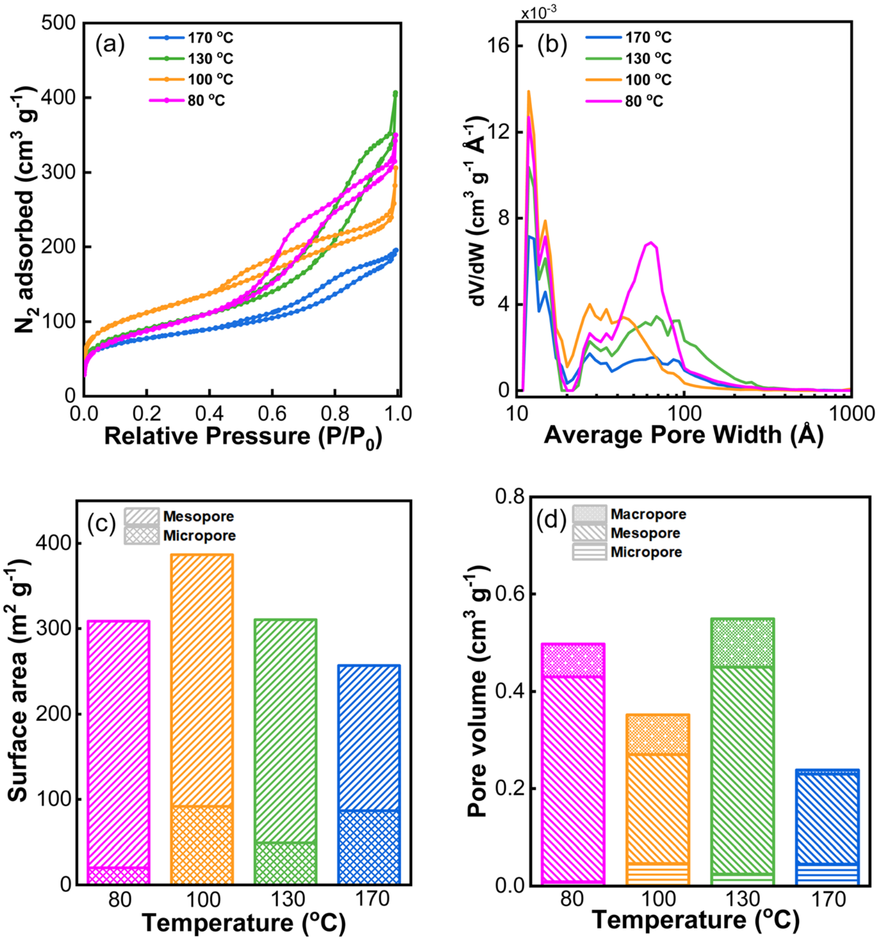

Fig. 9 Textural properties of P-MXene prepared by VPP as a function of temperature during intercalation. (a) N_2 adsorption–desorption isotherms; (b) pore-size distributions; (c) surface area partitioned into micro- and meso-contributions; (d) corresponding micro-, meso-, and macropore volumes. (Synthesis conditions: MXene/TEOS/DDA/H_2O = 1 : 6.4 : 0.8 : 10 (mass ratio), intercalation at 80, 100, 130, or 170 °C, and hydrolysis at 80 °C).

occurs (Fig. 10a). During freezing, solvent crystallization and subsequent sublimation induce structural rearrangement of the nanosheets. Although classical capillary stresses associated with liquid evaporation are minimized in freeze drying, van der Waals attractions between adjacent sheets and mechanical stresses generated during ice crystal formation can promote non-uniform interlayer collapse. Central regions of stacked domains experience greater compressive constraint due to limited edge relaxation, leading to heterogeneous gallery spacing. This process produces a wrinkled morphology with spatially varying interlayer distances (Fig. 2a and c). As reflected in the BET analysis (Fig. 3a and c), the resulting structure exhibits limited overall porosity, dominated by microporosity arising from wedge- or slit-like galleries between wrinkled and partially restacked layers, with only minor contributions from meso- and macroporosity.

Upon mixing MXene with DDA and heating above the melting point of DDA, molten DDA is drawn into the interlayer galleries by capillary forces to expand the interlayers apart. The intercalation process is further stabilized by hydrogen bonding

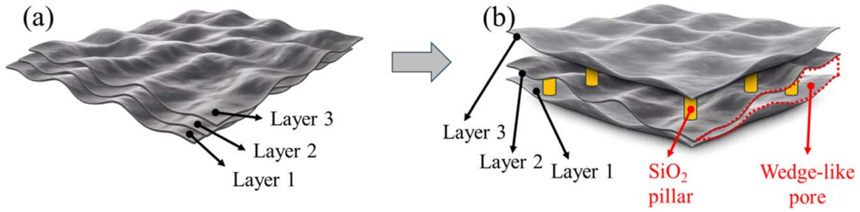

Fig. 10 Schematic illustration of stacked MXene layers with low porosity between layers after freeze drying (a) and with hierarchical wedge-like pores between layers after the VPP pillarization process (b).

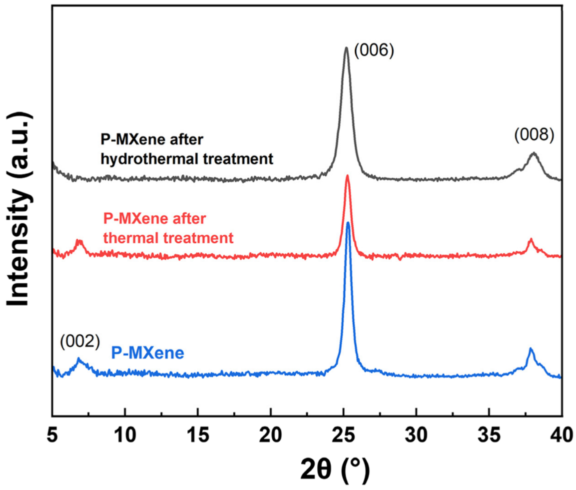

Fig. 11 XRD data of P-MXene after thermal and hydrothermal treatments. P-MXene synthesis conditions: MXene/DDA/TEOS/H_2O = 1 : 10 : 0.5 : 10 (mass ratio), intercalation at 100 °C, and hydrolysis at 80 °C. Thermal treatment was performed at 500 °C under N_2 (100 mL min^{-1}) for 24 h, while hydrothermal treatment was carried out at 500 °C under Ar (50 mL min^{-1}) for 24 h with 2 wt% steam.

between the –OH surface terminations of MXene and the –NH_2 groups of DDA. Following vapor-phase introduction of the silica precursor (TEOS), nucleation and condensation preferentially occur at regions of enhanced accessibility, surface functionalization (–OH and –O terminations), and structural defects. As a basic amine, DDA also catalyzes TEOS hydrolysis and condensation reactions with surface functional groups on the MXene sheets to form silica pillars. Because perimeter regions are more exposed to both molten DDA and vapor-phase TEOS diffusion, silica pillar growth proceeds more extensively at the sheet edges, resulting in taller pillars in these regions. In contrast, interior galleries experience diffusion-limited precursor access and stronger mechanical confinement, leading to shorter pillars and narrower interlayer spacing.

Thus, the resulting architecture consists of macro- and/or mesopores stabilized by taller edge pillars that prevent large-scale collapse, and micropores formed by interlayer galleries confined by shorter interior pillars or wrinkled regions in restacked MXene layers (Fig. 10b). The interconnection between the macro-, meso- and micropores forms wedge- or slit-like porosities. Overall, the final structure reflects a balance among capillary-induced collapse during drying, interlayer van der Waals attraction, swelling-induced expansion by DDA, and the mechanical rigidity of silica pillars. This interplay provides a mechanistic basis for the observed hierarchical pore distribution and explains the simultaneous emergence of macro-, meso- and microporosity without requiring intrinsic framework pore formation within individual MXene sheets.

3.6 Thermal and hydrothermal stability of P-MXene

Thermal and hydrothermal stability are important considerations for MXene-based materials in catalytic applications, particularly for thermal catalysis. In understanding these properties, we conducted both thermal and hydrothermal stability tests on the P-MXene material prepared from the VPP process. It is reported that MXene-based materials can undergo oxidation in air at temperatures above ∼350 °C.[9] Therefore, practical applications of MXene-based materials should generally be limited to temperatures below this temperature in oxidative environments. For completeness, we evaluated the stability of P-MXene under inert and hydrothermal conditions at elevated temperatures. For the thermal stability test, the sample (synthesis conditions: MXene/DDA/TEOS/H_2O = 1 : 10 : 0.5 : 10 (mass ratio), intercalation at 100 °C, and hydrolysis at 80 °C) was treated at 500 °C under flowing N_2 (100 mL min^{-1}) for 24 h. Hydrothermal stability was evaluated by exposing the sample to 500 °C under flowing 2% steam/98% Ar (50 mL min^{-1}) for 24 h. After treatment, N_2 adsorption–desorption isotherms and XRD patterns were collected.

For the hydrothermally treated sample, the XRD pattern (Fig. 11) shows disappearance of the (002) reflection, indicating significant disruption of the layered structure of P-MXene. This observation is consistent with the N_2 adsorption–desorption results, where both the surface area (Fig. 12c) and total pore volume (Fig. 12d) decreased after hydrothermal treatment. The structural degradation is likely due to collapse of the interlayer architecture upon prolonged exposure of the silica pillars to steam at high temperature. In contrast, for the thermally treated sample under dry N_2, the (002) peak was retained (Fig. 11), suggesting that the layered structure remained largely intact. Interestingly, thermal treatment resulted in an increase in surface area and pore volume (Fig. 12b–d). This enhancement may be attributed to further condensation or structural rearrangement of the silica pillars, reducing framework blockage and increasing accessible porosity. Additionally, trace oxygen impurities in the N_2 stream may have caused partial oxidation of carbon species in P-MXene, potentially generating additional micro- or macroporosity. Overall, these results indicate that P-MXene exhibits limited stability under high-temperature hydrothermal conditions, while it retains structural integrity more effectively under dry atmospheres. Nevertheless, prolonged exposure to high temperatures, even under inert conditions, can induce structural evolution. Therefore, catalytic applications of P-MXene should preferably be conducted at moderate temperatures to ensure structural stability.

3.7 P-MXene supported Ru catalyst for plastic hydrogenolysis

To evaluate the application potential of P-MXene synthesized *via* the VPP method, we employed it as a catalyst support for the chemical upcycling of plastics. Polyolefins, including polyethylene (PE) and polypropylene (PP), are thermoplastic materials that dominate the global plastics market due to their structurally simple yet highly versatile nature. They exhibit advantageous properties such as high strength-to-weight ratios, transparency, and excellent durability. However, the same chemical stability that underpins their utility also renders them resistant to depolymerization and degradation.[20] Ruthenium, a metal catalyst widely studied for polyolefin hydrogenolysis,[49]

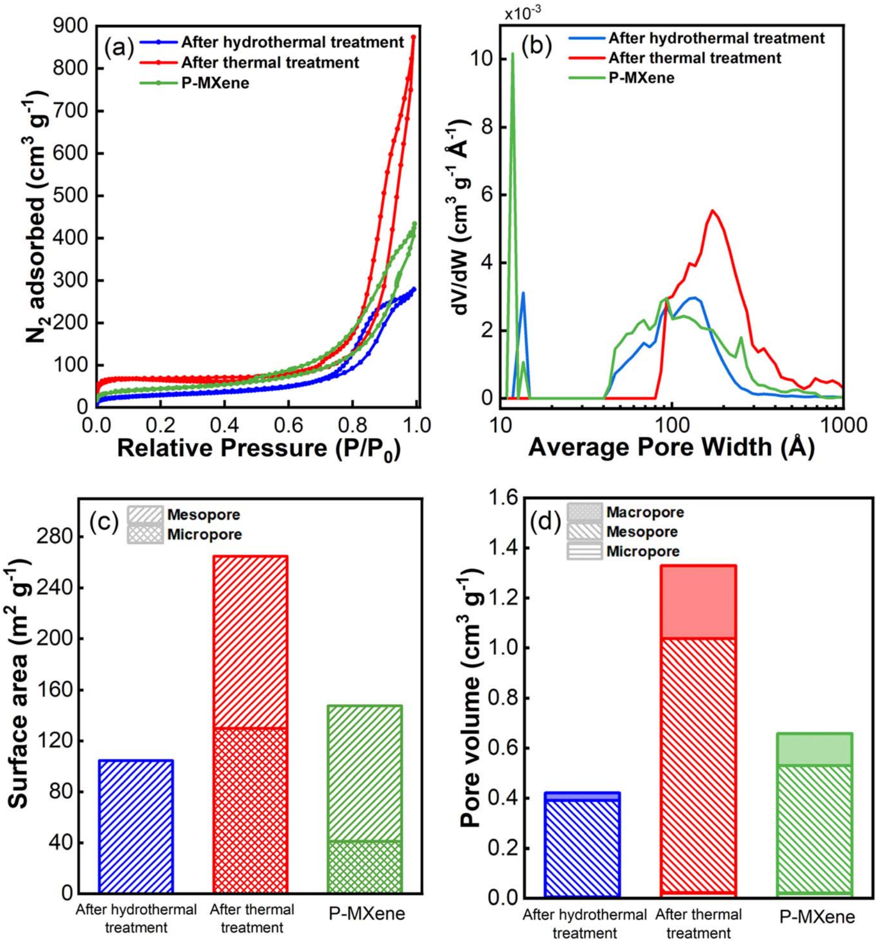

Fig. 12 Textural properties of P-MXene and P-MXene after thermal and hydrothermal treatments. (a) N_2 adsorption–desorption isotherms; (b) pore-size distributions; (c) surface area partitioned into micro- and meso-contributions; (d) corresponding micro-, meso-, and macropore volumes. P-MXene synthesis conditions: MXene/DDA/TEOS/H_2O = 1 : 10 : 0.5 : 10 (mass ratio), intercalation at 100 °C, and hydrolysis at 80 °C. Thermal treatment was performed at 500 °C under N_2 (100 mL min^{-1}) for 24 h, while hydrothermal treatment was carried out at 500 °C under Ar (50 mL min^{-1}) for 24 h with 2 wt% steam.

has shown superior catalytic performance, largely attributed to its lower activation energy barrier for the rate-determining C–C bond cleavage step.[50] Typical supports for Ru nanoparticles include TiO_2,[51] ZrO_2,[52] CeO_2,[53] and carbon materials.[54,55] Nevertheless, these catalyst systems often suffer from limited surface area and porosity, which restrict polymer–catalyst interfacial contact and hinder mass transport. To address this issue, Ru was selected as the active phase to prepare the P-MXene-supported Ru catalyst (Ru@P-MXene). For comparison, a MXene-supported Ru catalyst (Ru@MXene) was also synthesized and tested under identical reaction conditions. In both cases, the Ru loading was controlled at 5 wt%.

3.7.1 Catalyst properties. The morphologies of Ru particles in Ru@MXene and Ru@P-MXene catalysts were examined by HAADF-STEM imaging (Fig. 13). On the MXene support, Ru particles exhibited a spherical morphology (Fig. 13a). The particle size distribution histogram (inset in Fig. 13a) shows that the average particle size of Ru particles is ~1.9 nm. On the P-MXene support, no distinct Ru particles were observed (Fig. 13c). STEM-EDS elemental mapping confirmed the presence of Ru in Ru@P-MXene and revealed significantly improved dispersion compared to Ru@MXene (Fig. 13b and d). This enhanced dispersion is attributed to the increased surface area and mesopore volume generated by the VPP process.

The high-resolution Ru 3d XPS spectra of 5.0% Ru@MXene and 5.0% Ru@P-MXene were measured to provide insights into the coordination environment of Ru species. Deconvolution was performed using CasaXPS software following a previously reported method[56] to distinguish the Ru 3d signal from the C 1s spectrum.[56] As shown in Fig. 14, the C 1s spectra were deconvoluted into adventitious carbon species (C–C/C–H, ~284.8 eV), oxygenated carbons (C–O and O–C=O, ~286.2–288.9 eV), carbide-related peaks (C–Ti at ~282.0 eV), and Ru-related species overlapping with the C 1s region. The Ru 3d spectra were deconvoluted into Ru–Ru, Ru–O, and Ru–Cl states located around 280.4 eV, 280.9 eV, and 282.1 eV, respectively.[56] For the 5.0% Ru@MXene sample, the dominant features of the C–Ti peak confirm the preservation of the MXene carbide framework after Ru incorporation. Notably, Ru–Cl and Ru–O species are clearly resolved, suggesting that a substantial fraction of Ru

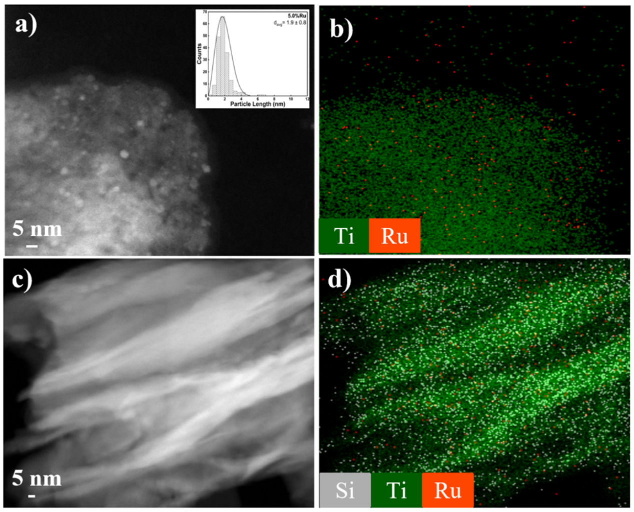

Fig. 13 HAADF-STEM images (a and c) and STEM-EDS mapping data (b and d) for Ru@MXene (a and b) and Ru@P-MXene (c and d), respectively. The inset in (a) is the Ru particle size histogram for the Ru@MXene sample. (P-MXene synthesis conditions: MXene/DDA/TEOS/H_2O = 1 : 10 : 0.5 : 10 (mass ratio), intercalation at 100 °C, and hydrolysis at 80 °C).

remains in the cationic state, derived from residual $RuCl_3$ precursors and oxidized Ru species stabilized on the MXene surface. The presence of Ru–Ru bonding contributions indicates partial reduction of Ru species to metallic Ru. This combination of metallic and oxidized Ru states supports the idea that the MXene substrate promotes both dispersion and partial reduction of Ru, while simultaneously stabilizing cationic species through surface terminations.[38,57,58] By contrast, the 5.0% Ru@P-MXene catalyst exhibits a markedly different spectral profile. While the characteristic C–Ti peak remains at ∼282.0 eV, confirming structural preservation of the MXene layers after pillarization, the Ru signal is dominated by Ru–O and Ru–Cl states, with little to no contribution from metallic Ru–Ru bonding. This indicates that Ru species are more finely dispersed and stabilized in oxidized form within the expanded interlayer environment created by silica pillars. The absence of metallic Ru features aligns with the observed smaller, more uniform Ru particle sizes from HAADF-STEM (Fig. 13c) in Ru@P-MXene compared to elongated Ru particles in Ru@MXene.

The high-resolution Ti 2p XPS spectra were deconvoluted into C–Ti–(O\O\O), C–Ti–(O\O\F), and C–Ti–(O\F\F) environments following Barsoum *et al.*[59] For 5.0% Ru@MXene, the presence of $TiO_{2-x}F_{2x}$ is also evident, though its contribution is moderate, suggesting partial oxidation of the surface during synthesis or handling. The coexistence of these states indicates that Ti atoms at the MXene surface are distributed among carbide-bonded and oxyfluoride environments. The multiple termination states likely facilitate anchoring of Ru species, stabilizing both cationic and metallic Ru as observed in the Ru 3d spectra. In contrast, the Ti 2p spectrum of 5.0% Ru@P-MXene is dominated by a strong $TiO_{2-x}F_{2x}$ component, with less pronounced contributions from mixed C–Ti–O/F states. The weaker intensity of carbide-related C–Ti peaks implies partial dilution of the Ti–C signal by the silica framework. This structural modification, while reducing the relative prominence of Ti–C bonding, creates more accessible sites, which can strongly stabilize dispersed Ru cations.

3.7.2 Hydrogenolysis of low-density polyethylene. The hydrogenolysis of low-density polyethylene (LDPE) was

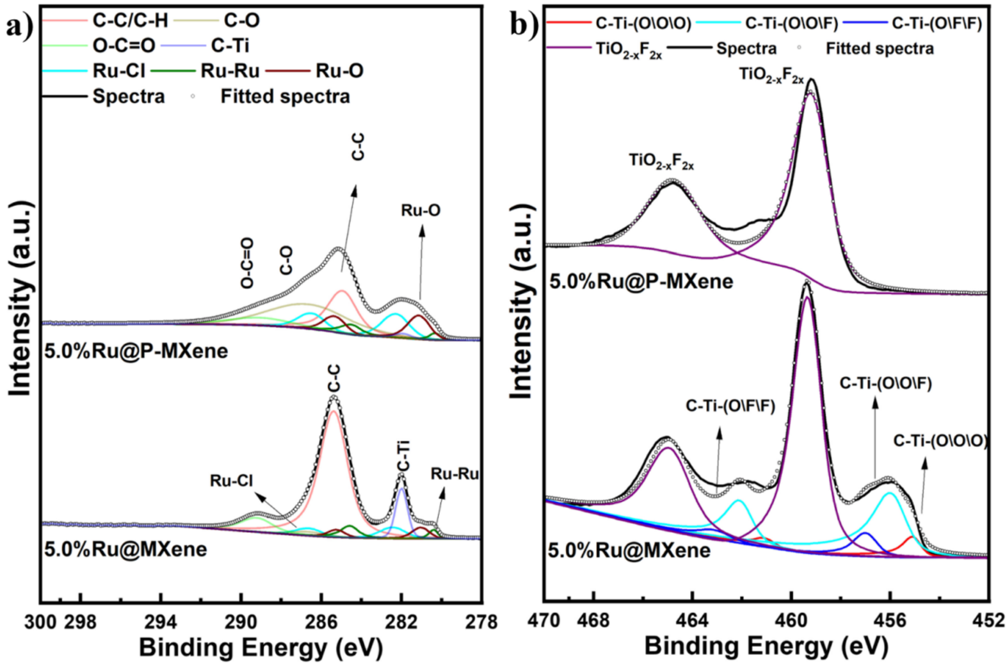

Fig. 14 XPS data for Ti 2p (a) and Ru 3d/C 1s (b) of Ru@MXene and Ru@P-MXene samples. (P-MXene synthesis conditions: MXene/DDA/TEOS/H_2O = 1 : 10 : 0.5 : 10 (mass ratio), intercalation at 100 °C, hydrolysis at 80 °C).

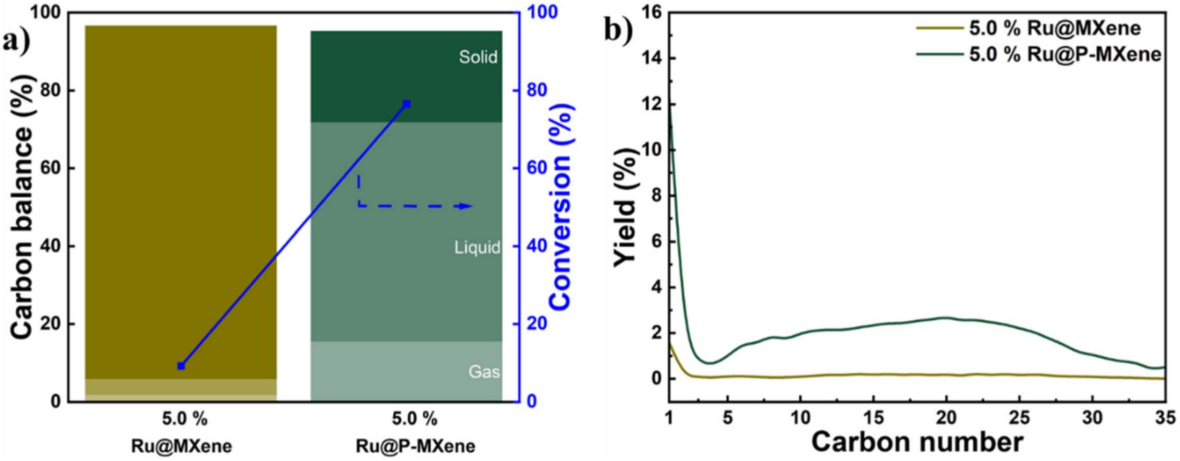

Fig. 15 Conversion and product selectivity (a) and product yield distribution (b) from LDPE hydrogenolysis over Ru@MXene and Ru@P-MXene catalysts. Reaction conditions: 250 °C, 30 bar H_2, LDPE feed/catalyst mass ratio = 20. The reaction time for Ru@MXene and Ru@P-MXene was 2 and 0.5 h, respectively. (P-MXene synthesis conditions: MXene/DDA/TEOS/H_2O = 1 : 10 : 0.5 : 10 (mass ratio), intercalation at 100 °C, and hydrolysis at 80 °C).

evaluated under identical conditions using Ru@P-MXene and Ru@MXene catalysts. As shown in Fig. 15a, Ru@MXene exhibited limited activity, achieving only 9.16% conversion after 2 hours. The product distribution consisted of 1.85% gas, 4.19% liquid, and 90.84% solid residue, with methane as the dominant gaseous product. In contrast, Ru@P-MXene delivered significantly enhanced performance, reaching 76.57% conversion within 0.5 hours. The product distribution shifted markedly toward more volatile products, with 15.46% gas, 56.36% liquid, and 23.43% solid (Fig. 15b). Methane again dominated the gaseous fraction, with a yield of 12.28%. For both catalysts, the high selectivity aligns with the well-established behavior of Ru-based catalysts in hydrogenolysis reactions.[54]

The low activity of Ru@MXene is attributed to the low BET surface area, small pore volume, and narrow pore sizes of the MXene support, which restrict accessibility to active sites and hinder mass transport. Moreover, Ru@MXene was synthesized *via* freeze-drying of MXene dispersed in a Ru precursor solution, a process that likely led to Ru species being intercalated between MXene layers.[60] By contrast, the superior activity of Ru@P-MXene stems from the significantly increased surface area, pore volume, and mesopore sizes provided by the pillared support. These textural improvements alleviate diffusion limitations and enhance the accessibility of polymer chains to Ru active sites. Collectively, these results highlight that P-MXene, with its optimized textural properties, more effectively harnesses the catalytic potential of MXene-based materials in heterogeneous thermal catalysis, an emerging application area for this promising class of 2D materials.

4. Conclusions

In summary, we developed a vapor-phase pillarization (VPP) strategy to engineer the pore architecture of mesoporous silica-pillared MXene (P-MXene). By optimizing the identity and loading of amine swelling agents, the amount of the silica precursor (TEOS), and the water content for hydrolysis, the resulting P-MXene exhibits expanded interlayer spacing, high surface area, and large mesopores, comparable to materials produced by liquid-phase pillarization. Moreover, by lowering the DDA loading while increasing TEOS, VPP-derived P-MXene attains more than twice the surface area of its LPP counterpart. The VPP route also improves precursor utilization and minimizes liquid waste, offering a more environmentally friendly, cost-effective, and operationally simple alternative to conventional liquid processing. To explore catalytic applications, P-MXene was used as a support for Ru nanoparticles (Ru@P-MXene) in polyethylene hydrogenolysis. The P-MXene support promotes highly dispersed Ru sites and better access for bulky polymer chains, enhancing mass transport in the molten phase and substantially increasing catalytic activity. Overall, this work advances MXene-based materials into new mesoporous architectures and underscores their promise as heterogeneous catalyst supports for heavy or bulky feedstocks such as plastics.

Author contributions

Song Luo: conceptualization, formal analysis, investigation, methodology, writing – original draft, writing – review & editing; Ali Kamali: formal analysis, investigation, writing – original draft; Joshua Little: investigation, writing – review & editing; Po-Yen Chen: supervision, writing – review & editing; Yeonsu Kwak: investigation, writing – review & editing; Dion Vlachos: supervision, writing – review & editing; Akash Warty: investigation; Hyunjik Kim: investigation; Jong K. Keum: investigation; Ke Zhang: funding acquisition, project administration, supervision; John Yang: funding acquisition, project administration, supervision; Dongxia Liu: conceptualization, formal analysis, methodology, writing – original draft, writing – review & editing, supervision, funding acquisition, project administration.

Conflicts of interest

The authors have filed a provisional patent application related to the materials/processes described in this manuscript.

Data availability

The data supporting this article have been included as part of the supplementary information (SI). Supplementary information: VPP-pillared MXene without DDA or DDA separated from MXene, property of MAX material, kinetics for DDA intercalation, thermogravity analysis (TGA) of MXene material, LDPE hydrogenolysis over Ru@P-MXene compared to P-MXene and Ru/C, textural properties of PMXene synthesized by VPP approach, detailed experimental and analytical procedures for LDPE hydrogenolysis. See DOI: https://doi.org/10.1039/d5ta09345g.

Acknowledgements

This work was supported as part of the Center for Plastics Innovation, an Energy Frontier Research Center funded by the U.S. Department of Energy, Office of Science, Basic Energy Sciences under Grant Number DE-SC0021166 and U. S. National Science Foundation under Grant number NSF-PFI-MCA-2220588. This work was also supported through a research agreement with Saudi Aramco (CW53673). Small-angle X-ray scattering experiments were conducted at the Center for Nanophase Materials Sciences (CNMS), a U.S. Department of Energy (DOE) Office of Science User Facility, under user proposal CNMS2024-B-02687. This research also utilized resources at the Spallation Neutron Source (SNS), a DOE Office of Science User Facility operated by the Oak Ridge National Laboratory.

References

1 M. Naguib, M. Kurtoglu, V. Presser, J. Lu, J. Niu, M. Heon, L. Hultman, Y. Gogotsi and M. W. Barsoum, Two-Dimensional Nanocrystals Produced by Exfoliation of Ti_3AlC_2, *Adv. Mater.*, 2011, **23**(37), 4248–4253.

2 M. Ghidiu, M. R. Lukatskaya, M.-Q. Zhao, Y. Gogotsi and M. W. Barsoum, Conductive Two-Dimensional Titanium Carbide 'Clay' with High Volumetric Capacitance, *Nature*, 2014, **516**(7529), 78–81.

3 K. R. G. Lim, M. Shekhirev, B. C. Wyatt, B. Anasori, Y. Gogotsi and Z. W. Seh, Fundamentals of MXene Synthesis, *Nat. Synth.*, 2022, **1**(8), 601–614.

4 C. Wang, Y. Yang, S. Zhang, Z. Yang, Y. Song, Z. Tang, T.-Y. Sang, F. Wan, S. Sun and W. Chen, The Impact of Surface Functional Groups on MXene Anode Protective Layer in Aqueous Zinc-Ion Batteries: Understanding the Mechanism, *J. Energy Storage*, 2024, **94**, 112360.

5 T. Shimada, N. Takenaka, Y. Ando, M. Otani, M. Okubo and A. Yamada, Relationship between Electric Double-Layer Structure of MXene Electrode and Its Surface Functional Groups, *Chem. Mater.*, 2022, **34**(5), 2069–2075.

6 B. Zhu, K. Wang, H. Gao, Q. Wang, X. Pan and M. Fan, Functional Group Modification and Bonding Characteristics of Ti3C2 MXene-Organic Composites from First-Principles Calculations, *ChemPhysChem*, 2021, **22**(16), 1675–1683.

7 J. Zhao, J. Wen, J. Xiao, X. Ma, J. Gao, L. Bai, H. Gao, X. Zhang and Z. Zhang, Nb2CTx MXene: High Capacity and Ultra-Long Cycle Capability for Lithium-Ion Battery by Regulation of Functional Groups, *J. Energy Chem.*, 2021, **53**, 387–395.

8 P. A. Maughan, S. Arnold, Y. Zhang, V. Presser, N. Tapia-Ruiz and N. Bimbo, In Situ Investigation of Expansion during the Lithiation of Pillared MXenes with Ultralarge Interlayer Distance, *J. Phys. Chem. C*, 2021, **125**(38), 20791–20797.

9 P. A. Maughan, V. R. Seymour, R. Bernardo-Gavito, D. J. Kelly, S. Shao, S. Tantisriyanurak, R. Dawson, S. J. Haigh, R. J. Young, N. Tapia-Ruiz and N. Bimbo, Porous Silica-Pillared MXenes with Controllable Interlayer Distances for Long-Life Na-Ion Batteries, *Langmuir*, 2020, **36**(16), 4370–4382.

10 A. Syed, I. Ali, S. Maqbool, M. Yousaf, I. Hussain, K. Zhang, S. A. Khan and S. Rizwan, Efficient Electrochemical Performance of Asymmetric Supercapacitor Based on Nitrogen-Doped Nb2CTx MXene in an Alkaline Electrolyte, *Nano Res. Energy*, 2025, **4**, e9120164.

11 R. Al Shaikh, A. Al-Othman, P. Nancarrow, M. Tawalbeh and A. Shamayleh, MXene-Based Materials for Proton-Exchange Membrane Fuel Cell Applications, *Cell Rep. Phys. Sci.*, 2026, **7**(1), 103053.

12 N. H. Solangi, N. M. Mubarak, R. R. Karri, S. A. Mazari and J. R. Koduru, Recent Development of Graphene and MXene-Based Nanomaterials for Proton Exchange Membrane Fuel Cells, *Int. J. Hydrog. Energy*, 2024, **73**, 905–931.

13 N. K. Chaudhari, H. Jin, B. Kim, D. San Baek, S. H. Joo and K. Lee, MXene: An Emerging Two-Dimensional Material for Future Energy Conversion and Storage Applications, *J. Mater. Chem. A*, 2017, **5**(47), 24564–24579.

14 J. Pang, R. G. Mendes, A. Bachmatiuk, L. Zhao, H. Q. Ta, T. Gemming, H. Liu, Z. Liu and M. H. Rummeli, Applications of 2D MXenes in Energy Conversion and Storage Systems, *Chem. Soc. Rev.*, 2019, **48**(1), 72–133.

15 T. Thomas, S. Bontha, A. Bishnoi and P. Sharma, MXene as a Hydrogen Storage Material? A Review from Fundamentals to Practical Applications, *J. Energy Storage*, 2024, **88**, 111493.

16 S. Nahirniak, A. Ray and B. Saruhan, Challenges and Future Prospects of the MXene-Based Materials for Energy Storage Applications, *Batteries*, 2023, **9**(2), 126.

17 M. W. Boey, M. Ahmad, J. Sun, S. K. Ravi, X. Wang, M. U. Farid and A. K. An, Agent Free Pillaring Engineering of Interlayer Spacing of Ti3C2 MXene Layers for Energy Conversion and Photothermal Desalination, *Chem. Eng. J.*, 2025, **519**, 165120.

18 M. Qin, Y. Yao, J. Mao, C. Chen, K. Zhu, G. Wang, D. Cao and J. Yan, Pillar Effect Induced by Ultrahigh Phosphorous/Nitrogen Doping Enables Graphene/MXene Film with Excellent Cycling Stability for Alkali Metal Ion Storage, *J. Energy Chem.*, 2024, **93**, 146–156.

19 W. Bai, L. Shi, Z. Li, D. Liu, Y. Liang, B. Han, J. Qi and Y. Li, Recent Progress on the Preparation and Application in Photocatalysis of 2D MXene-Based Materials, *Mater. Today Energy*, 2024, **41**, 101547.

20 A. Kamali, J. M. Little, S. Luo, A. Chen, A. Warty, A. Bhowmick, J. Moncada, E. P. Jahrman, B. C. Vance, J. K. Keum, T. J. Woehl, P.-Y. Chen, D. G. Vlachos and D. Liu, Plastic-Waste Hydrogenolysis over Two-Dimensional MXene-Supported Ruthenium Catalysts with Tunable Interlayer Spacing, *Chem Catal.*, 2025, **5**(9), 101459.

21 H. Wang, J. Ding, H. Zhao, Q. Chu, J. Zhu and J. Wang, Robust and Reprocessable Biorenewable Polyester Nanocomposites *In Situ* Catalyzed and Reinforced by Dendritic MXene@CNT Heterostructure, *Nano-Micro Lett.*, 2025, **17**(1), 161.

22 M. Naguib, J. Come, B. Dyatkin, V. Presser, P.-L. Taberna, P. Simon, M. W. Barsoum and Y. Gogotsi, MXene: A Promising Transition Metal Carbide Anode for Lithium-Ion Batteries, *Electrochem. Commun.*, 2012, **16**(1), 61–64.

23 Z. Lin, D. Sun, Q. Huang, J. Yang, M. W. Barsoum and X. Yan, Carbon Nanofiber Bridged Two-Dimensional Titanium Carbide as a Superior Anode for Lithium-Ion Batteries, *J. Mater. Chem. A*, 2015, **3**(27), 14096–14100.

24 O. Mashtalir, M. Naguib, V. N. Mochalin, Y. Dall'Agnese, M. Heon, M. W. Barsoum and Y. Gogotsi, Intercalation and Delamination of Layered Carbides and Carbonitrides, *Nat. Commun.*, 2013, **4**(1), 1716.

25 K. Gupta, J. Park, S. H. Im and W.-S. Kim, Efficient Adsorption of Antibiotics Using MXene Nanosheet Delaminated by Taylor Vortex Flow, *Sep. Purif. Technol.*, 2025, **357**, 130095.

26 K. Diedkova, I. Roslyk, N. Kanas, L. Grine, V. Deineka, A. Blacha-Grzechnik, M. Boroduskis, I. Iatsunskyi, B. Anastaziak, A. Konieva, P. Shubin, W. Simka, M. Truhins, O. Sulaieva, I. Yanko, V. Zahorodna, G. Stojanovic, O. Gogotsi, Y. Gogotsi and M. Pogorielov, Effects of Etching and Delamination on Biocompatibility of Ti-Based MXenes, *ACS Appl. Mater. Interfaces*, 2025, **17**(34), 47919–47937.

27 A. Raman, J. S. Jayan, B. D. S. Deeraj, M. Srivastava, K. Joseph and A. Saritha, Delamination of MXene Using Biomolecule: An Effective Strategy toward the Utilization of Delaminated MXene as Fillers in Polymer Composites, *Polym. Compos.*, 2025, **46**(4), 3193–3207.

28 S. Wang, Y. Li, X. Zhou, Y. Yang and G. Chen, Lithiophilic SiO $_2$ Nanoparticle Pillared MXene Nanosheets for Stable and Dendrite-Free Lithium Metal Anodes, *J. Mater. Chem. A*, 2023, **11**(37), 20165–20173.

29 J. Luo, W. Zhang, H. Yuan, C. Jin, L. Zhang, H. Huang, C. Liang, Y. Xia, J. Zhang, Y. Gan and X. Tao, Pillared Structure Design of MXene with Ultralarge Interlayer Spacing for High-Performance Lithium-Ion Capacitors, *ACS Nano*, 2017, **11**(3), 2459–2469.

30 S. Zhang, H. Ying, P. Huang, J. Wang, Z. Zhang, Z. Zhang and W.-Q. Han, Ultrafine Sb Pillared Few-Layered Ti $_3$ C $_2$ T $_x$ MXenes for Advanced Sodium Storage, *ACS Appl. Energy Mater.*, 2021, **4**(9), 9806–9815.

31 L. Wei, K. Song, W. Wu, S. Holdren, G. Zhu, E. Shulman, W. Shang, H. Chen, M. R. Zachariah and D. Liu, Vapor-Phase Strategy to Pillaring of Two-Dimensional Zeolite, *J. Am. Chem. Soc.*, 2019, **141**(22), 8712–8716.

32 P. Lu, S. Ghosh, M. Dorneles De Mello, H. S. Kamaluddin, X. Li, G. Kumar, X. Duan, M. Abeykoon, J. A. Boscoboinik, L. Qi, H. Dai, T. Luo, S. Al-Thabaiti, K. Narasimharao, Z. Khan, J. D. Rimer, A. T. Bell, P. Dauenhauer, K. A. Mkhoyan and M. Tsapatsis, Few-Unit-Cell MFI Zeolite Synthesized Using a Simple Di-quaternary Ammonium Structure-Directing Agent, *Angew. Chem., Int. Ed.*, 2021, **60**(35), 19214–19221.

33 S. Cao, K. Zhang, B. Hanna and E. Al-Sayed, Methane Oxidation by Green Oxidant to Methanol over Zeolite-Based Catalysts, *Chin. Chem. Lett.*, 2022, **33**(4), 1757–1762.

34 X. Wang, Y. Ma, Q. Wu, Y. Wen and F.-S. Xiao, Zeolite Nanosheets for Catalysis, *Chem. Soc. Rev.*, 2022, **51**(7), 2431–2443.

35 K. Kałahurska, W. Pajerski, A. Kotarba, M. Kubů, Y. Zhang, M. Mazur, J. Přech, G. Jajko, W. Makowski, W. J. Roth and B. Gil, Platinum Nanoparticles Supported on Zeolite MWW Nanosheets Prepared *via* Homogeneous Solution Route, *Catal. Today*, 2022, **390–391**, 335–342.

36 T. Zhou, D. Zhang, Y. Liu, Y. Sun, T. Ji, S. Huang and Y. Liu, Construction of Monodispersed Single-Crystalline Hierarchical ZSM-5 Nanosheets *via* Anisotropic Etching, *J. Energy Chem.*, 2022, **72**, 516–521.

37 J. M. Little, J. Sun, A. Kamali, A. Chen, A. C. Leff, Y. Li, L. K. Borden, T. U. Dissanayake, D. Essumang, B. O. Oseleononmen, D. Liu, T. J. Woehl and P.-Y. Chen, Noble Metal Ion-Directed Assembly of 2D Materials for Heterostructured Catalysts and Metallic Micro-Texturing, *Adv. Funct. Mater.*, 2023, **33**(30), 2215222.

38 J. M. Little, A. Chen, A. Kamali, T. S. Akash, C.-S. Park, D. Liu, S. Das, T. J. Woehl and P.-Y. Chen, Drying Controlled Synthesis of Catalytic Metal Nanocrystals Within 2D-Material Nanoconfinements, *Adv. Funct. Mater.*, 2025, **35**(6), 2414746.

39 L. Wei, K. Song, W. Wu, S. Holdren, G. Zhu, E. Shulman, W. Shang, H. Chen, M. R. Zachariah and D. Liu, Vapor-Phase Strategy to Pillaring of Two-Dimensional Zeolite, *J. Am. Chem. Soc.*, 2019, **141**(22), 8712–8716.

40 E. Ruiz-Hitzky, M. Ounis, M. K. Younes and J. Pérez-Carvajal, Silica–$Ti_3C_2T_x$ MXene Nanoarchitectures with Simultaneous Adsorption and Photothermal Properties, *Materials*, 2024, **17**(17), 4273.

41 X. Li, Y. Tang, L. Liu, Y. Zhang, R. Sheng and Y. NuLi, Ti_3C_2 MXene with Pillared Structure for Hybrid Magnesium-Lithium Batteries Cathode Material with Long Cycle Life and High Rate Capability, *J. Colloid Interface Sci.*, 2022, **608**, 2455–2462.

42 O.-Y. Kwon, H.-S. Shin and S.-W. Choi, Preparation of Porous Silica-Pillared Layered Phase: Simultaneous Intercalation of Amine-Tetraethylorthosilicate into the H $^+$ -Magadiite and Intragallery Amine-Catalyzed Hydrolysis of Tetraethylorthosilicate, *Chem. Mater.*, 2000, **12**(5), 1273–1278.

43 K.-W. Park, J. H. Jung, J. D. Kim, S.-K. Kim and O.-Y. Kwon, Preparation of Mesoporous Silica-Pillared H+-Titanosilicates, *Microporous Mesoporous Mater.*, 2009, **118**(1–3), 100–105.

44 Z. Dong, D. Ding, T. Li and C. Ning, Black Si-Doped TiO_2 Nanotube Photoanode for High-Efficiency Photoelectrochemical Water Splitting, *RSC Adv.*, 2018, **8**(11), 5652–5660.

45 T. Hu, J. Wang, H. Zhang, Z. Li, M. Hu and X. Wang, Vibrational Properties of Ti_3C_2 and $Ti_3C_2T_2$ (T = O, F, OH) Monosheets by First-Principles Calculations: A Comparative Study, *Phys. Chem. Chem. Phys.*, 2015, **17**(15), 9997–10003.

46 M. Shekhirev, C. E. Shuck, A. Sarycheva and Y. Gogotsi, Characterization of MXenes at Every Step, from Their Precursors to Single Flakes and Assembled Films, *Prog. Mater. Sci.*, 2021, **120**, 100757.

47 K. S. W. Sing, Reporting Physisorption Data for Gas/Solid Systems with Special Reference to the Determination of Surface Area and Porosity (Recommendations 1984), *Pure Appl. Chem.*, 1985, **57**(4), 603–619.

48 J. Rouquerol, D. Avnir, C. W. Fairbridge, D. H. Everett, J. M. Haynes, N. Pernicone, J. D. F. Ramsay, K. S. W. Sing and K. K. Unger, Recommendations for the Characterization of Porous Solids (Technical Report), *Pure Appl. Chem.*, 1994, **66**(8), 1739–1758.

49 C. Jia, S. Xie, W. Zhang, N. N. Intan, J. Sampath, J. Pfaendtner and H. Lin, Deconstruction of High-Density Polyethylene into Liquid Hydrocarbon Fuels and Lubricants by Hydrogenolysis over Ru Catalyst, *Chem Catal.*, 2021, **1**(2), 437–455.

50 A. Almithn and D. Hibbitts, Comparing Rate and Mechanism of Ethane Hydrogenolysis on Transition-Metal Catalysts, *J. Phys. Chem. C*, 2019, **123**(9), 5421–5432.

51 P. A. Kots, S. Liu, B. C. Vance, C. Wang, J. D. Sheehan and D. G. Vlachos, Polypropylene Plastic Waste Conversion to Lubricants over Ru/TiO2 Catalysts, *ACS Catal.*, 2021, **11**(13), 8104–8115.

52 C. Wang, T. Xie, P. A. Kots, B. C. Vance, K. Yu, P. Kumar, J. Fu, S. Liu, G. Tsilomelekis, E. A. Stach, W. Zheng and D. G. Vlachos, Polyethylene Hydrogenolysis at Mild Conditions over Ruthenium on Tungstated Zirconia, *JACS Au*, 2021, **1**(9), 1422–1434.

53 Y. Nakaji, M. Tamura, S. Miyaoka, S. Kumagai, M. Tanji, Y. Nakagawa, T. Yoshioka and K. Tomishige, Low-Temperature Catalytic Upgrading of Waste Polyolefinic Plastics into Liquid Fuels and Waxes, *Appl. Catal. B Environ.*, 2021, **285**, 119805.

54 J. E. Rorrer, G. T. Beckham and Y. Román-Leshkov, Conversion of Polyolefin Waste to Liquid Alkanes with Ru-Based Catalysts under Mild Conditions, *JACS Au*, 2021, **1**(1), 8–12.

55 J. A. Sun, P. A. Kots, Z. R. Hinton, N. S. Marinkovic, L. Ma, S. N. Ehrlich, W. Zheng, T. H. I. Epps, L. T. J. Korley and D. G. Vlachos, Size and Structure Effects of Carbon-Supported Ruthenium Nanoparticles on Waste Polypropylene Hydrogenolysis Activity, Selectivity, and Product Microstructure, *ACS Catal.*, 2024, **14**(5), 3228–3240.

56 D. J. Morgan, Resolving Ruthenium: XPS Studies of Common Ruthenium Materials, *Surf. Interface Anal.*, 2015, **47**(11), 1072–1079.

57 Y. Long, Y. Tao, T. Shang, H. Yang, Z. Sun, W. Chen and Q.-H. Yang, Roles of Metal Ions in MXene Synthesis, Processing and Applications: A Perspective, *Adv. Sci.*, 2022, **9**(12), 2200296.

58 Q. Zhang, J. Wang, Q. Yu, Q. Li, R. Fan, C. Li, Y. Fan, C. Zhao, W. Cheng, P. Ji, J. Sheng, C. Zhang, S. Xie, G. Henkelman and H. Li, Metal/MXene Composites *via in Situ* Reduction, *Nat. Synth.*, 2025, **4**(2), 252–261.

59 V. Natu, M. Benchakar, C. Canaff, A. Habrioux, S. Célérier and M. W. Barsoum, A Critical Analysis of the X-Ray Photoelectron Spectra of Ti3C2Tz MXenes, *Matter*, 2021, **4**(4), 1224–1251.

60 Y. Deng, T. Shang, Z. Wu, Y. Tao, C. Luo, J. Liang, D. Han, R. Lyu, C. Qi, W. Lv, F. Kang and Q. Yang, Fast Gelation of $Ti_3\ C_2\ T_x$ MXene Initiated by Metal Ions, *Adv. Mater.*, 2019, **31**(43), 1902432.